PAPER





Geological and sea level controls on offshore freshened groundwater in a rift basin: Gulf of Corinth, Greece

Senay Horozal¹ · Aaron Micallef^{1,2} · Michele De Biase³ · Francesco Chidichimo⁴

Received: 6 August 2024 / Accepted: 4 August 2025 © The Author(s) 2025

Abstract

Offshore freshened groundwater (OFG) is a potential unconventional water source for coastal cities, but its spatial distribution, emplacement mechanisms and the geological factors influencing OFG migration and preservation remain poorly constrained. The Gulf of Corinth (GOC) in Greece, an active continental rift, presents a unique study area where pore-water freshening has been documented through scientific drilling. In this study, the spatial distribution, emplacement mechanisms and controls on OFG has been investigated in the GOC sediments by integrating core physical properties, lithostratigraphy, 2D seismic reflection data and 2D hydrogeological modelling. The freshened water extends from ca. 20 to 600–700 m below seafloor (mbsf) in the central subbasin and from ca. 15 to 150 mbsf in the eastern subbasin of the Alkyonides Gulf. This freshened water in the gulf sediments is attributed to meteoric recharge during glacial periods. A 2D hydrogeological model of salinity changes over the past 800,000 years confirms that the deep basin's freshened water is a remnant from sea-level lowstands. The results indicate that both glacial and interglacial sediments stored freshwater, with salinity variations occurring independently of total porosity, likely because of vertical diffusion of fluids across sediments deposited during multiple interglacial and glacial cycles. The laterally continuous seismic units in the gulf basin may contain up to 250 km³ of freshened groundwater. This study offers new insights into the occurrence and distribution of freshened groundwater in rift basins, highlighting the role of long-term sea-level fluctuations in groundwater freshening, and providing a comprehensive model for groundwater storage capacity in such environments.

Keywords Gulf of Corinth rift basin \cdot Offshore freshened groundwater \cdot Petrophysical and hydrogeological modeling \cdot Diffusive salt transport \cdot Greece

Published in the special issue "Advances in understanding offshore freshened groundwater".

 ⊠ Senay Horozal senayhorozal@gmail.com

Published online: 19 September 2025

- Department of Geoscience, University of Malta, Msida, Malta
- Monterey Bay Aquarium Research Institute, Moss Landing, USA
- ³ CNR-IRPI, Research Institute for Geo-Hydrological Protection, Rende, Italy
- Department of Environmental Engineering, University of Calabria, Rende, Italy

Introduction

Many coastal cities are facing severe water shortages because of increased population, water contamination, and climate change impacts (e.g., Cohen et al. 2010; Berndt and Micallef 2019; Micallef et al. 2021; Sheng et al 2023). Offshore freshened groundwater (OFG), stored in subseafloor sediments and rocks with salinity levels lower than seawater, has been proposed as an unconventional water source to address these challenges (e.g., Bakken et al. 2012; Person and Micallef 2022). Despite its estimated global volume (ca. $5-10\times10^5$ km³; Post et al. 2013; Micallef et al. 2021), key questions remain regarding its recharge and discharge, if/how the terrestrial and offshore systems are connected, and how these systems will evolve in a changing climate (Micallef et al. 2021). These knowledge gaps persist primarily because of the technical challenges associated with acquiring field data on OFG (Lofi et al. 2013).



Various mechanisms have been proposed for OFG emplacement in continental margins, including active meteoric recharge through onshore-offshore aquifer connections (e.g., Michael et al. 2016; Gustafson et al. 2019), meteoric recharge during sea-level lowstands (e.g., Zhang et al. 2018; Thomas et al. 2019), sub-glacial and pro-glacial injection (e.g., Person et al. 2012), diagenesis (e.g., Moore and Saffer 2001), and decomposition of gas hydrates (e.g., Lin et al. 2016). Meteoric recharge is the most commonly reported OFG emplacement process in the literature (72.8%), with recharge during lowstands being the most prevalent (33.4%) (Micallef et al. 2021).

Previous studies have shown contrasting results on the role of geology in OFG storage, with both high-permeability units, such as coarse-grained sediments (Hathaway et al. 1979), and low-permeability formations such as fine-grained clay intervals and limestones (e.g., Lofi et al. 2013; Haroon et al. 2021), acting as reservoirs. Additionally, OFG has been identified in fractured karstic rocks (Varma and Michael 2012; Morgan et al. 2018) and channel sands (Davies 1997; Micallef et al. 2020). The original depositional architecture strongly controls permeability distribution, which affects OFG flow, distribution, and flow. OFG bodies are often hosted in coarse sediments beneath fine-grained aquitards, which trap freshwater deposited during sea-level lowstands

(Bratton 2007; Micallef et al. 2020). The connectivity of permeable and confining strata further controls OFG extent. For instance, permeable zones can extend OFG offshore, while features such as faults, paleochannels, and submarine canyons influence flow, mixing, and discharge (Groen et al. 2000; Lofi et al. 2013; Morgan et al. 2018). In many of the aforementioned OFG investigations, lithological features (e.g., permeable vs. non-permeable units), depositional structures (e.g., paleochannels, clinoforms), and tectonic elements (e.g., faults) have been shown to either facilitate fluid flow or act as barriers to migration within sedimentary strata. However, the understanding of the geological controls on OFG systems remains limited, largely because of a lack of fundamental constraints on lithologies, material properties, ages, and pore fluid conditions. There has been limited integration of seismic reflection data with petrophysical and geochemical analyses to comprehensively evaluate the geological controls on OFG distribution and flow.

In this study, these knowledge gaps are addressed in the Gulf of Corinth (GOC; Fig. 1), an active rift zone. OFG has never been previously investigated in this area, with recharge potentially originating from all directions. The study combines seismic reflection data, petrophysical analysis from the International Ocean Discovery Program (IODP) Expedition 381 (McNeill et al. 2019a; Fig. 2), and numerical

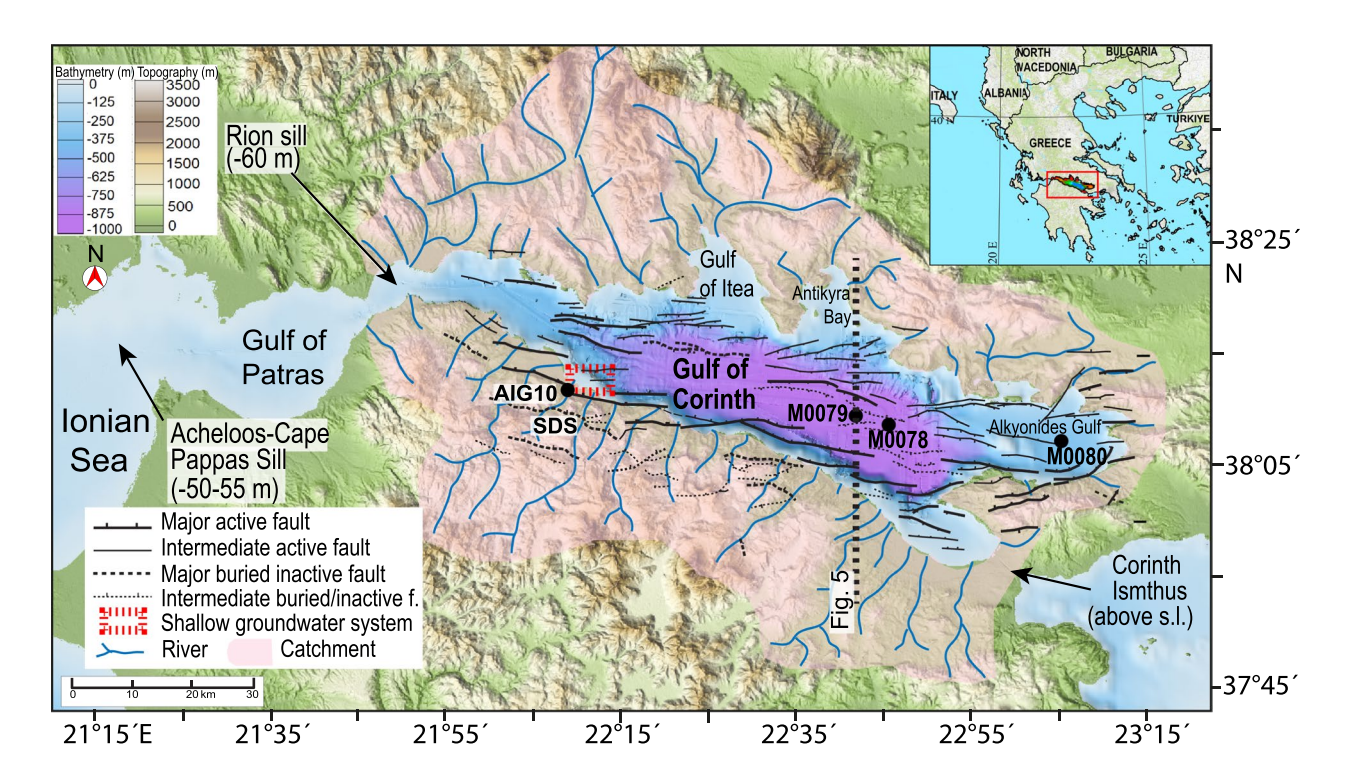


Fig. 1 Physiographic map of the Gulf of Corinth (GOC) and its surroundings, showing topography and mapped faults onshore and offshore, which are predominantly oriented in E–W direction (modified from Bell et al. 2009; McNeill et al. 2019a). Black circles denote the location of the IODP Expedition 381 drilling sites M0079, M0078

and M0080, and the AIG10 well. The dashed red rectangular marks the area of previously documented freshened groundwater discharge (Christodoulou et al. 2003). The red box on the index map bounds the study area. Elevation and bathymetry are measured relative to sea level (s.l.)



groundwater modelling to achieve the following key objectives: (1) quantification of the volume and spatial extent of the OFG in the GOC, (2) establishment of the origin and emplacement mechanism of the OFG, and (3) evaluation of the controls on OFG distribution.

Regional and geological setting

Regional setting

The GOC is a young (< 5 Ma) active rift basin located in central Greece, characterized by an extension rate of up to 15 mm/year (Bell et al. 2011; Fig. 1). The basin has an elongated asymmetric shape with a surface area of 2500 km², extending for ca. 130 km in a west-east direction and ca. 20 km in a north-south direction. The southern continental shelf is narrow (< 1 km) with steep slopes (14–18°), whereas the northern continental shelf is broader (up to 12 km) and has gentler slopes (1-2°; Fig. 2; Poulos et al. 1996). The central part of the GOC is the deepest, with water depths exceeding 900 m (Fig. 2). Hydrologically, the GOC is connected to the Ionian Sea and Mediterranean Sea via the Rion Sill in the west (60 m below sea level, mbsl) and the Corinth Canal in the east (55 mbsl; Bell et al. 2008; Perissoratis et al. 2000; Fig. 1). During Quaternary glacial periods, a drop in sea level separated the GOC from the Mediterranean Sea (McNeill et al. 2019a). The surrounding catchment area exceeds 5,000 km², with the catchment network stabilizing at ca. 400–600 ka and coinciding with the rift's present-day geometry (Ford et al. 2013). The northward-draining catchments have a steeper gradient compared to the south- or west-draining streams (Fig. 1).

Structural setting

Offshore seismic reflection profiles reveal numerous E–W striking, N- and S-dipping normal faults forming horst and graben structures (Fig. 1; Bell et al. 2009; Nixon et al. 2016). Basement depth is greatest in the central rift (~ 3 km) and decreases toward the east and west (Bell et al. 2009). The GOC's two major depocenters, 20–50-km long, formed before 400 ka, with a single 80-km-long depocenter controlled by N-dipping faults since then (Bell et al. 2009). Onshore, faults south of the GOC are up to 20 km long, with displacements of several kilometers (Fig. 1; Gawthorpe et al. 2017).

Sedimentology

Sediments from the GOC were sampled during IODP expedition 381, which drilled three sites: M0078, M0079, and M0080 (Figs. 1 and 2; McNeill et al. 2019a). At all sites, alternating interglacial and glacial subunits were identified in the upper lithostratigraphy. Interglacial intervals predominantly consist of homogeneous green-grey bioturbated mud with marine microfauna, interbedded with isolated sandy deposits, typically 0.5 to 20 cm thick, composed mainly of very fine-grained sands. These intervals are interpreted as being deposited in deep marine conditions with occasional

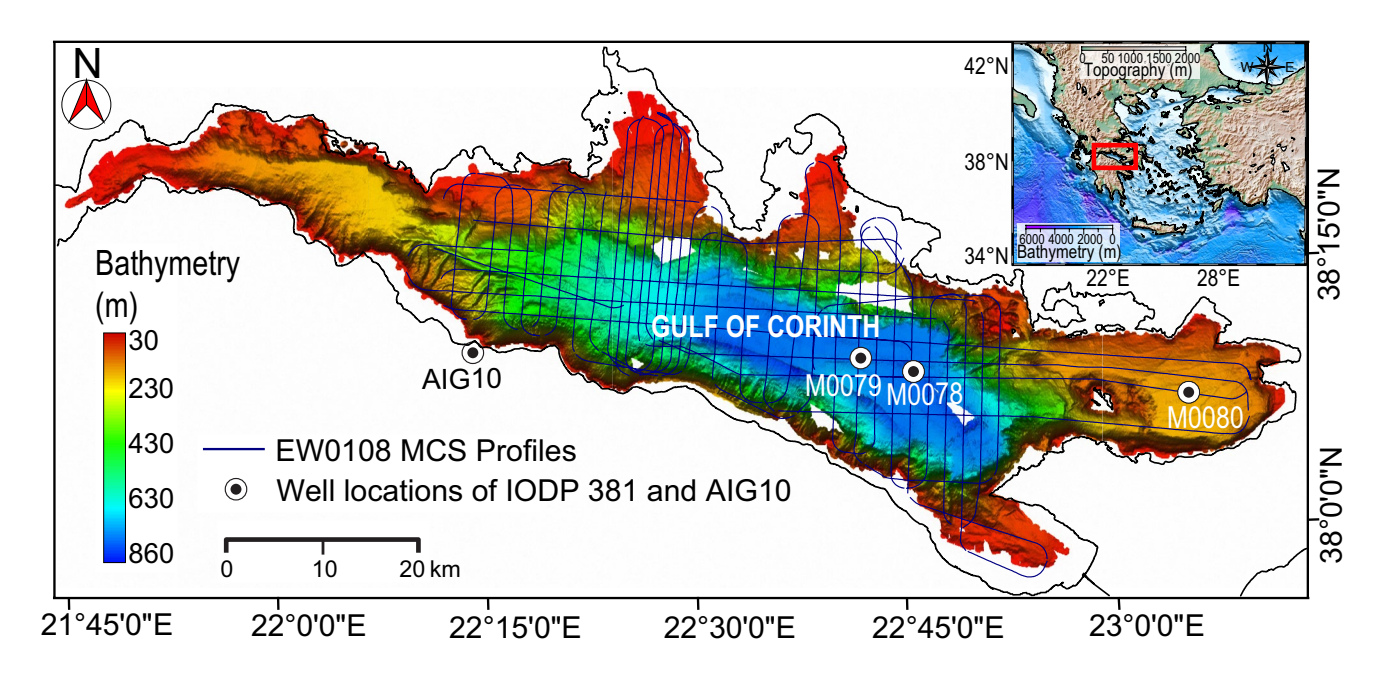


Fig. 2 Bathymetric map of the GOC shown with the locations of multi-channel seismic (MCS) reflection profiles (track lines) and the IODP Expedition 381 drilling sites M0079A, M0078A and M0080A and the AIG10 onshore well



occurrences of turbidite deposits. Glacial intervals are composed of facies associations dominated by beds of laminated mud lacking marine microfauna (McNeill et al. 2019a, b), with the abundant occurrence of turbidite deposits. Sedimentation rates during glacial periods were 2-7 times higher than during interglacial periods, likely because of reduced vegetation cover (McNeill et al. 2019b; Gawthorpe et al. 2022). The grain size analysis from site M0079A shows that glacial and interglacial sediments have nearly identical grain size frequency distributions (Kang et al. 2022). However, the marine sediments from interglacial periods are slightly coarser in nature, which can be attributed to changes in current circulation associated with the opening of the Isthmia Strait (Fig. 1; Kang et al. 2022). The presence of this open strait likely altered the shallow water current circulation in the southeastern area of the basin, facilitating the transport of shallow sediments to the deep-water basin axis.

The origin of sediments in the GOC during both glacial and interglacial periods may include hemipelagic suspension settling (McNeill et al. 2019a; Gawthorpe et al. 2022), seismically induced gravitational mass flows sourced from basin slopes (Sergiou et al. 2016), gravitational collapse of ancient deltas along the southern margin induced by seismic activity (Ferentinos et al. 1988; Lykousis et al. 2007a, b; Gawthorpe et al. 2017), and hypopycnal plumes and lofted turbidity currents (Gawthorpe et al. 2022) in a deep water rift-axis setting.

Deltaic deposits, including lowstand and highstand deltas, are particularly common along the southern margin of the GOC, where major rivers are located (Gawthorpe et al. 2017). Previous studies from the GOC (e.g., Ferentinos et al. 1988; Lykousis et al. 2007a, b; Gawthorpe et al. 2017) have documented evidence of the gravitational collapse of ancient deltas, such as scarps along their edges and associated slumps/slides (Lykousis et al. 2007a, b). These delta-front mass failures are transported downslope via high-density turbidity flows into the basin, resulting in the deposition of coarse-grained sediments (Ferentinos et al. 1988).

At site M0078 (central GOC), 610 m of sediment were recovered with 87% core recovery. Lithostratigraphy is divided into two units, with unit 1 further subdivided into 16 subunits, alternating between interglacial (odd-numbered) and glacial (even-numbered) intervals (Table S1 of the electronic supplementary material (ESM); McNeill et al. 2019a).

Site M0079, in the central Corinth Basin, recovered ca. 705 m of sediment with 86.65% recovery, with the oldest sediments dating to ca. 750 ka. Lithostratigraphy is divided into two units, with unit 1 subdivided into 16 subunits, following the same pattern as site M0078 (Table S1 of the ESM; McNeill et al. 2019a).

Site M0080, located in the Alkyonides Gulf, cored ca. 634 m of sediments with 84% recovery. Lithostratigraphy includes four units, with unit 1 subdivided

into 11 subunits on the basis of alternations between dominantly bioturbated, homogeneous, and poorly bedded greenish-gray to gray mud, and laminated mud beds (Table S1 of the ESM; McNeill et al. 2019a).

Stratigraphy

The seismic stratigraphy of the GOC reveals a synrift succession up to ca. 2.5-km thick, divided into two seismic units: SU1 (lower) and SU2 (upper), separated by an angular unconformity (Unconformity–U or H7 in this study; Fig. 3; McNeill et al. 2019a; Bell et al. 2008; Taylor et al. 2011; Nixon et al. 2016). SU1 consists of discontinuous low-amplitude reflections while SU2 exhibits alternating low- and high-amplitude reflections, interpreted as lowstand lacustrine and highstand marine sequences, respectively (e.g., Sachpazi et al. 2003; Lykousis et al. 2007a, b; Bell et al. 2008, 2009; Taylor et al. 2011; Nixon et al. 2016). The base of SU2 is estimated as ca. 600 ka (Nixon et al. 2016), while biostratigraphy from the IODP cruise suggests an age of ca. 770 ka (McNeill et al 2019a).

Data

Multibeam echosounder data

Multibeam bathymetric data (EW0108 Cruise Report, 2001; McNeill et al. 2005) were collected during EW0108 survey using a Hydrosweep DS-2 sonar system (Fig. 2). The data were manually edited after sound-velocity corrections on the basis of four XBTs (salinity, depth, temperature). A 55-m grid, also including digitized points from nautical charts to fill gaps in the shallow gulf areas, was generated.

Multi-channel seismic reflection data

Multi-channel seismic reflection (MCS) data (EW0108; Cruise Report 2001; McNeill et al. 2005) were collected aboard the R/V Maurice Ewing in 2001 (EW0108; Fig. 2). The seismic source used a generator-injector air gun (5.2 M/m³ primary pulse) at 50-m intervals. Each shot recorded 6384 ms of data at a 4 ms sample rate. Seismic Lines in the Gulf of Itea were recorded with 240-channel, 6 km-long streamers at 25-m group spacing (23 profiles), while other Lines used 240 channel, 3 km-long streamers with 12.5-m group intervals (26 profiles). The MCS data were processed at the University of Hawaii using ProMAX and SeisWorks, including geometry setup and binning, editing, muting, deconvolution, NMO and velocity analysis, brute stack, time-varying band pass filter and post-stack time migration (Taylor et al. 2011).



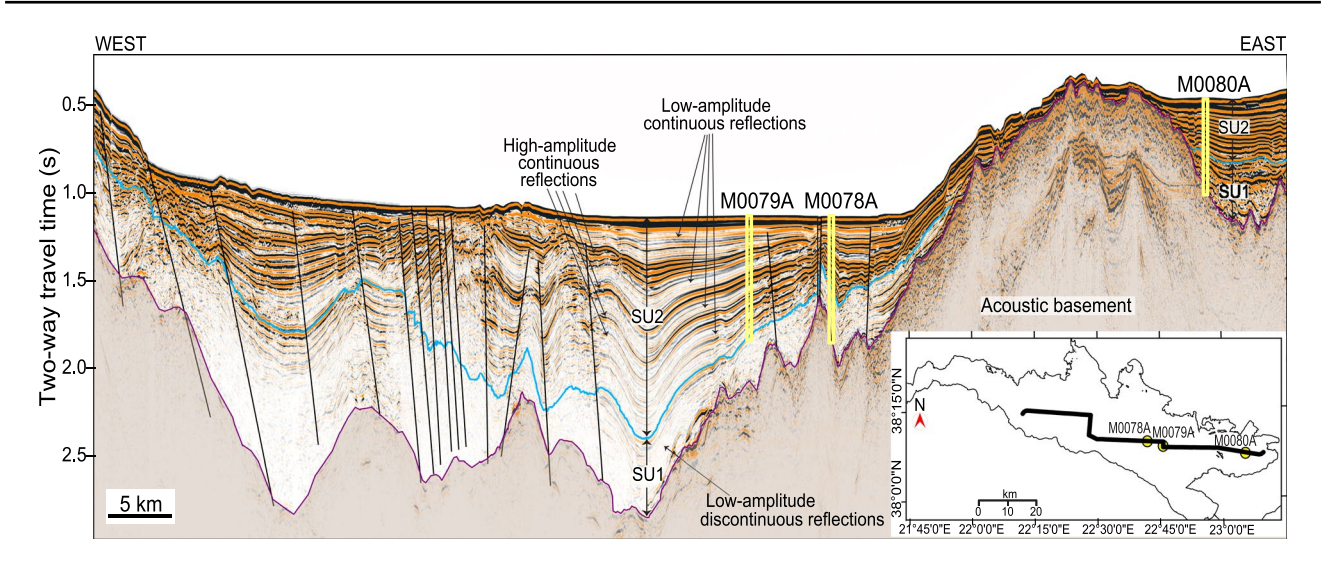


Fig. 3 E–W trending arbitrary seismic profile crossing the IODP drilling sites, showing the general seismic stratigraphy of the GOC. Two distinct seismic units, seismic unit 1 (SU1) and seismic unit 2 (SU2), are discernible, separated by a prominent angular unconformity or seismic boundary (H7, marked by blue horizon). SU1 exhibits

low-amplitude discontinuous reflections, while SU2 features alternating high- and low-amplitude continuous seismic reflections. Numerous faults offset the sedimentary strata, with some extending into the seafloor. The location of arbitrary seismic section is shown by bold black line in the index map

Offshore drilling sites and petrophysical data

Offshore drilling data from sites M0078A, M0079A and M0080A (Figs. 1 and 2; IODP Expedition 381 Scientists 2020) were acquired during IODP Expedition 381 in 2018 (McNeill et al. 2019a, b). Petrophysical data include wireline logs of gamma ray (GR), P-wave seismic velocity, natural gamma ray (NGR), moisture and density (MAD) porosity (total porosity), and wet bulk density. Time and depth (T-D) charts were also used for the seismic-to-well tie. Physical properties, MAD total porosity and wet bulk density were obtained from offshore and onshore whole cores, split cores, and discrete samples (McNeill et al. 2019a). Pore-water samples were collected using rhizons or squeeze cakes and analyzed for geochemistry, including alkalinity, ammonium, pH, chlorinity and salinity with only salinity being used in this study. Salinity sampling intervals ranged from < 10 m in the uppermost sections to 20 m in the deeper sections.

Methodology

Seismic and well data analyses

A total of 14 horizons were mapped from seismic reflection data, including the top of the acoustic basement, seafloor, and horizons H1–H7, which define seismic unit (SU) boundaries (Fig. 3; Table S1 of the ESM). In the central subbasin, these SU boundaries are named from older to younger as H7, base and top of H6 to H2, and

H1 (Table S1 of the ESM). This nomenclature follows the IODP Expedition 381 scientific reports (McNeill et al. 2019a) and Nixon et al. (2016).

Biostratigraphic ages from site M0079 were used to assign ages to seismic unit boundaries (Table S1 of the ESM; McNeill et al. 2019a, b). However, the ages of SU boundaries in the eastern gulf remain uncertain because of the lack of biostratigraphic data at site M0080 (McNeill et al. 2019a).

In the central subbasin, 12 seismic units were assigned between these boundaries. These are labeled SU1-1 within SU1 and SU2-1 to SU2-12 within SU2 (Table S1 of the ESM). The central and the eastern parts of the GOC basin are separated by a basement high (Fig. 3), so the seismic interpretation, mapping, and volumetric calculation were done separately for the central and the eastern subbasins. Seismic and lithological units also differ between these basins. In the eastern subbasin, H1 and the top of the horizons between H2 and H6 are not defined, and seismic units are named SU1-1 in SU1, and SU2-1 and SU2-6 in SU2 (Table S1 of the ESM).

Lithostratigraphic units in the central subbasin were correlated with seismic units (Table S1 of the ESM). There are 17 subunits distributed in two seismic units described in the cores of sites M0078A and M0079A. However, M0079A is considered the best fit when correlating lithological subunits to seismic units because of the strong correlation between well and seismic data (Fig. S1 of the ESM). In the eastern gulf, lithostratigraphy consists of four units (U1–U4), further subdivided into 22 subunits (Table S1 of the ESM).



Site M0079A										
Seismic units	Horizons	Seismic subunits	Porosity mean (%)	Salinity mean (g/L or psu)	Age (ka)	Thickness (m)	Age gap (ka)	Diffusion time (ka)	Min. hydraulic conductivity (m/s)	Max. hydraulic conductivity (m/s)
Unit 1	AB	SU1-1	34.6	7.4	2500	319.3	1727	5470.3	7.1×10^{-10}	4.5×10^{-9}
Unit 2	H1	SU2-12	51.7	28.5	13	36.5	13	50.8	4.6×10^{-9}	2.8×10^{-8}
	H2_top	SU2-11	47.4	10.9	70	116.7	57	531.9	2.9×10^{-9}	1.8×10^{-8}
	H2_bottom	SU2-10	51.0	11.5	129	31.1	59	35.1	4.3×10^{-9}	2.7×10^{-8}
	H3_top	SU2-9	43.8	12.5	168	82.9	39	291.4	1.9×10^{-9}	1.2×10^{-8}
	H3_bottom	SU2-8	47.5	13.1	245	50.9	77	104.3	2.9×10^{-9}	1.8×10^{-8}
	H4_top	SU2-7	42.1	12.5	276	59.4	31	155.2	1.7×10^{-9}	8.9×10^{-9}
	H4_bottom	SU2-6	45.3	10.4	335	30.4	59	37.7	2.5×10^{-9}	1.6×10^{-8}
	H5_top	SU2-5	41.6	7.6	366	39.4	31	69.2	1.5×10^{-9}	9.6×10^{-9}
	H5_bottom	SU2-4	43.3	8.6	420	16.9	54	12.2	1.8×10^{-9}	1.1×10^{-8}
	H6_top	SU2-3	38.9	11.2	436	8.09	16	175.8	1.2×10^{-9}	7.2×10^{-9}
	H6_bottom	SU2-2	41.7	6.4	575	56.1	139	139.9	1.7×10^{-9}	1.0×10^{-8}
	H7	SU2-1	38.7	8.9	773	81.8	198	320.0	1.3×10^{-9}	7.3×10^{-9}

Construction of time structure and isopach maps and volumetric estimation of OFG

Thickness maps of seismic units were constructed from isopachs converted to depth using the time-depth (T-D) chart from site M0079A. For volumetric estimation of OFG, the mean total porosity and salinity values for each seismic unit were calculated (Tables S2 and S3 of the ESM). Using these porosity values and isopach maps, volumes were determined via the volumetric module of IHS Kingdom Suite software for the central and eastern subbasins (Tables S2 and S3 of the ESM). Volumetric calculations assumed a laterally homogeneous distribution of freshened groundwater, using constant average salinity and total porosity values from site M0079A, with sediment pores fully saturated with water.

3D petrophysical modelling

3D total porosity and salinity models (e.g. Lipparini et al. 2023) for the central and eastern subbasins of the GOC were developed using core petrophysical data from three sites. Models were created with a grid size of 50 m in the X and Y directions, covering the three main sites in the GOC. The modelling process involved zone modelling (creating horizons, zones, and layers), upscaling and property modelling.

Fourteen horizons, including the seabed and top of the acoustic basement, define the top and base surfaces. Thirteen seismic units were created from the top and base of these horizons, and each zone was divided into 10 internal layers. After model setup, total porosity and salinity values from sites M0078A, M0079A, and M0080A were upscaled using arithmetic averaging. The upscaled properties were populated in the zones using the sequential Gaussian simulation (SGS) tool of Petrel petrophyscial modelling.

Vertical diffusive salt transport

Vertical diffusive salt transport times in the offshore deep site M0079A were calculated on the basis of the density of saline water using Cl^- ions. The diffusion time (t) is given by $t = L^2/D$, where D is the diffusion coefficient in a porous medium, and L is the unit thickness (Lofi et al. 2013). The effective diffusion coefficient was estimated as a function of porosity and tortuosity for Cl⁻ ions in porous media. These calculations account for aquifer properties such as total porosity and hydraulic conductivity, which influence the rate of vertical diffusive salt transport. The hydraulic conductivity (K) (or permeability k) of the aguifer units were considered to be high where their values exceeded defined thresholds. These properties were considered to be high where the values were defined to be $K > 1 \times 10^{-6}$ m/s



Fig. 4 2D geological model domain created by integrating onshore (Giurgea et al. 2004; Loveless 2013) with offshore geology data, illustrating discretization settings and seismic subunits derived from the geological model. The light blue area indicates the range of water-level variation over the last 800 ka

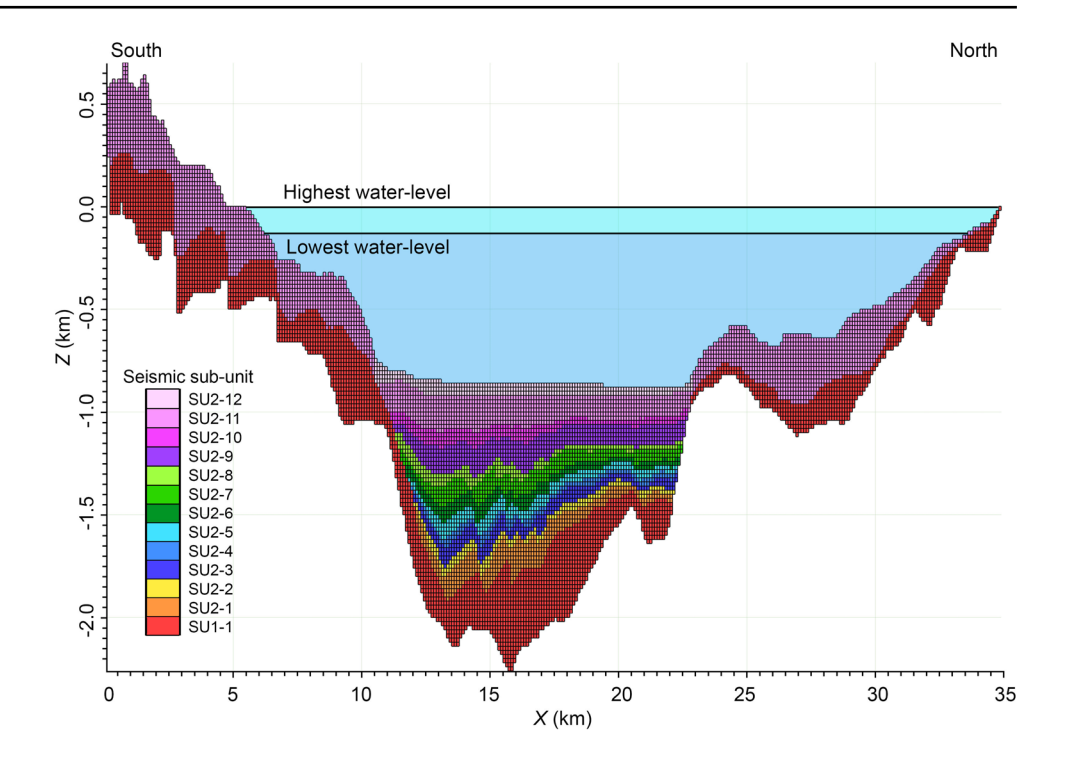


Table 2 Sea level cycles, used as input hydraulic heads in the model, and associated depositional environments in the Gulf of Corinth

Cycle No.	Cycle age range (ka)	Environment/Deposition	Water condition	Hydraulic head (m)
1	800–773	Isolated/glacial	Mixed (7.4 g/L) ^a	-129.7
2	773–626	Isolated/glacial	Fresh (0 g/L)	-7.47
3	626-575	Marine/interglacial	Saline (38 g/L or psu) ^b	-29.59
4	575-535	Isolated/glacial	Fresh	-7.92
5	535-467	Marine/interglacial	Saline	-60.99
6	467-453	Isolated/glacial	Fresh	-59.24
7	453-436.4	Marine/interglacial	Saline	-94.65
8	436.4-420	Isolated/glacial	Fresh	-112.9
9	420-366	Marine/interglacial	Saline	-61.24
10	366-335	Isolated/glacial	Fresh	-60.11
11	335-276	Marine/interglacial	Saline	-59.21
12	276-245	Isolated/glacial	Fresh	-60.0
13	245-168	Marine/interglacial	Saline	-56.68
14	168-129	Isolated/glacial	Fresh	-58.58
15	129-70	Marine/interglacial	Saline	-61.77
16	70–13	Isolated/glacial	Fresh	-60.68
17	13–0	Marine/seafloor	Saline	0.0

^aInitial water salinity condition

(or k > 103 mD), or low where the values were defined to be $K < 1 \times 10^{-8}$ m/s (k < 1 mD) (Lofi et al. 2013), respectively. Calculations for the maximum limit of K show medium-to-low k of units, ranging from 2.8×10^{-8} and 4.5×10^{-9} m/s. Mean total porosities within each seismic unit were used for the calculations, which are presented in Table 1.

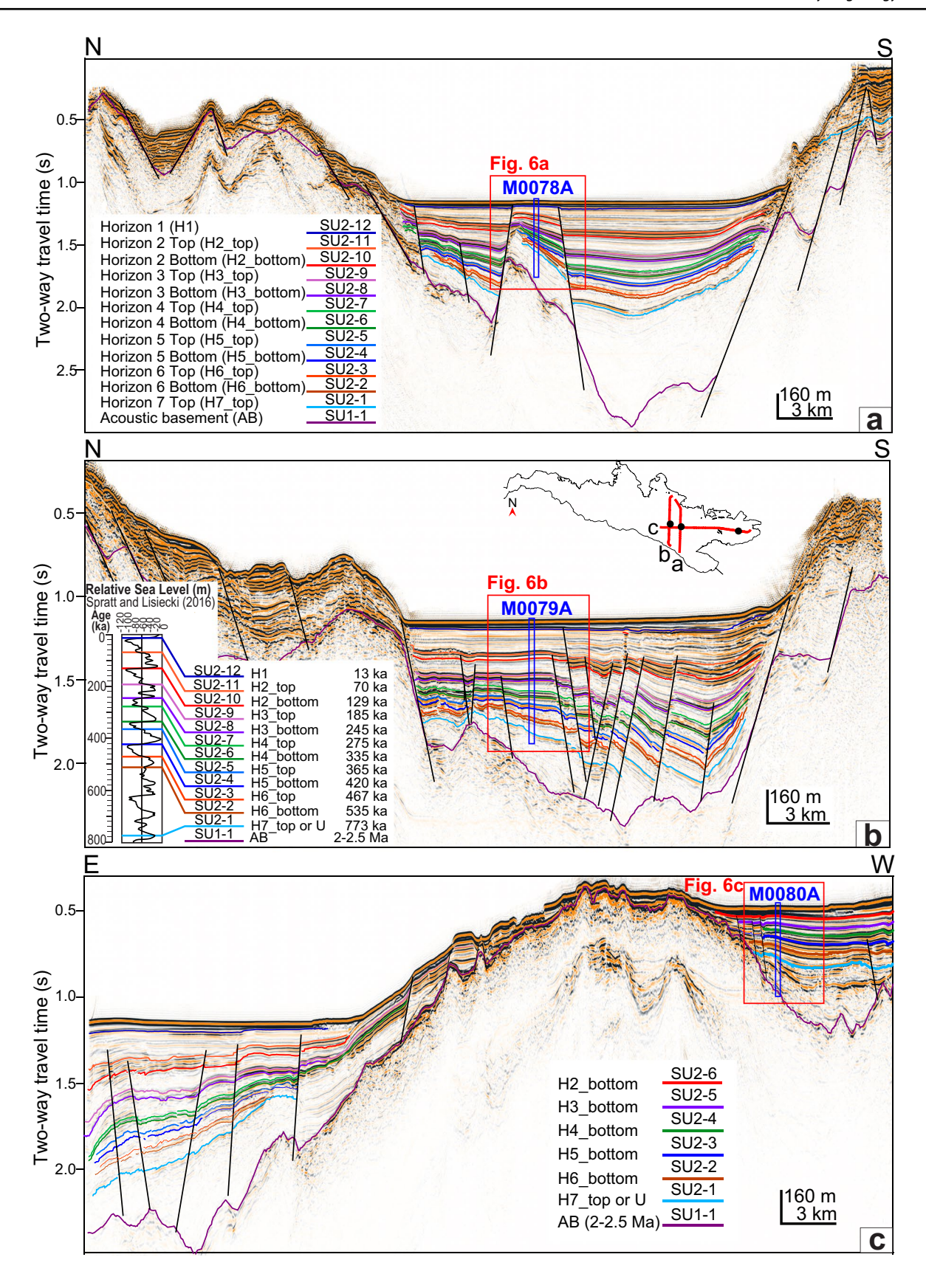
Groundwater model

2D geological model construction

A 2D geological model was developed by integrating the geology of the onshore southern margin, including



^bAssumed seawater salinity





▼Fig. 5 Interpreted multi-channel seismic (MCS) profiles crossing IODP sites: a M0078A, b M0079A, and c M0080A. A total of 13 seismic units (SU1-1 and SU2-1 to SU2-12) are identified and mapped in the central basin (a−b) bound by 13 horizons, namely H1, H2_top to H6_top, H2_bottom to H6_bottom, H7 or U, and the top of the acoustic basement (e.g., Nixon et al. 2016; McNeill et al. 2019a). In the eastern subbasin (c), separated by a basement high from the central basin, seven seismic units (SU1-1 and SU2-1 to SU2-6) bounded by seven horizons are defined. Age correlation from the IODP drilling study (McNeill et al. 2019b) and the relative sea level curve (Spratt and Lisiecki 2016) suggests that most odd-numbered seismic units (SU2-5 to SU2-11) correspond to glacial intervals, while even numbered units (SU2-4 to SU2-12) correlate with interglacial periods (b). Locations of seismic profiles are shown with red bold lines on the base map

deltaic deposits constructed from outcrops and core samples of well AIG10 (Giurgea et al. 2004; Loveless 2013), with offshore seismic reflection data. The model was oriented in the south-north direction to align with the southern tip of the seismic line crossing IODP site M0079A. The northern margin model, ending at the exposed basement rock above sea level, was also interpolated. The hydraulic conductivity values for the sedimentary units along the southern onshore margin (gray and dark gray unit in Table S4 of the ESM) were assigned on the basis of the laboratory measurements reported by Loveless (2013). For deep basin sediments, hydraulic conductivities were calculated from total porosities and D_{10} grain size (input 0.4 and 1 µm for high and low permeability units) using the Kozeny-Carman equation (Kozeny 1927; Carman 1956). For the northern shelf sediments, identified as deltaic on the seismic reflection data, hydraulic conductivity values from the southern AIG10 well were applied (Table S4 of the ESM).

Groundwater model layout

The variable-density groundwater model SEAWAT (Langevin et al. 2008) was used to reproduce the 2D vertical cross-section running through the GOC in a north-south direction (Fig. 4). Onshore and offshore profiles, derived from the geological reconstruction, were combined for this purpose. Simulations under transient conditions were performed to investigate processes that led to the porewater salinity anomalies observed beneath the seabed. The model domain, based on the morphological and geological reconstruction, covers a V-shaped area of $35 \times 3 \text{ km}^2$, extending from the seabed to the impermeable bedrock. It is vertically discretized by a mesh of $100\text{-m} \times 20\text{-m}$ -rectangular elements, resulting in 150 horizontal layers (Fig. 4). Depending on whether the hydraulic head value is above

or below the top of a specific cell during simulations, the model determines whether to treat it as a confined element or not.

Model parameters

The spatial distribution of porosity and K was assigned on the basis of the lithologies reconstructed in the geological model (Table 1). Vertical hydraulic conductivity (K) values were set to a tenth of the horizontal K values in order to account for anisotropy (e.g., Lemieux et al. 2015; De Biase et al. 2021). In the absence of direct measurements, specific yield and specific storage values for the sediment in the study area were estimated on the basis of typical parameters of materials with similar hydraulic conductivity and grain size characteristics (Lv et al. 2021; Chowdhury et al. 2022). These values were 0.02 for specific yield and 8.7×10^{-4} (L/m) for specific storage.

The empirical power law developed by Schulze-Makuch (2005) was used to account for the solute local velocity variations in the flow direction, and hence to define a value for the longitudinal dispersivity α [L]:

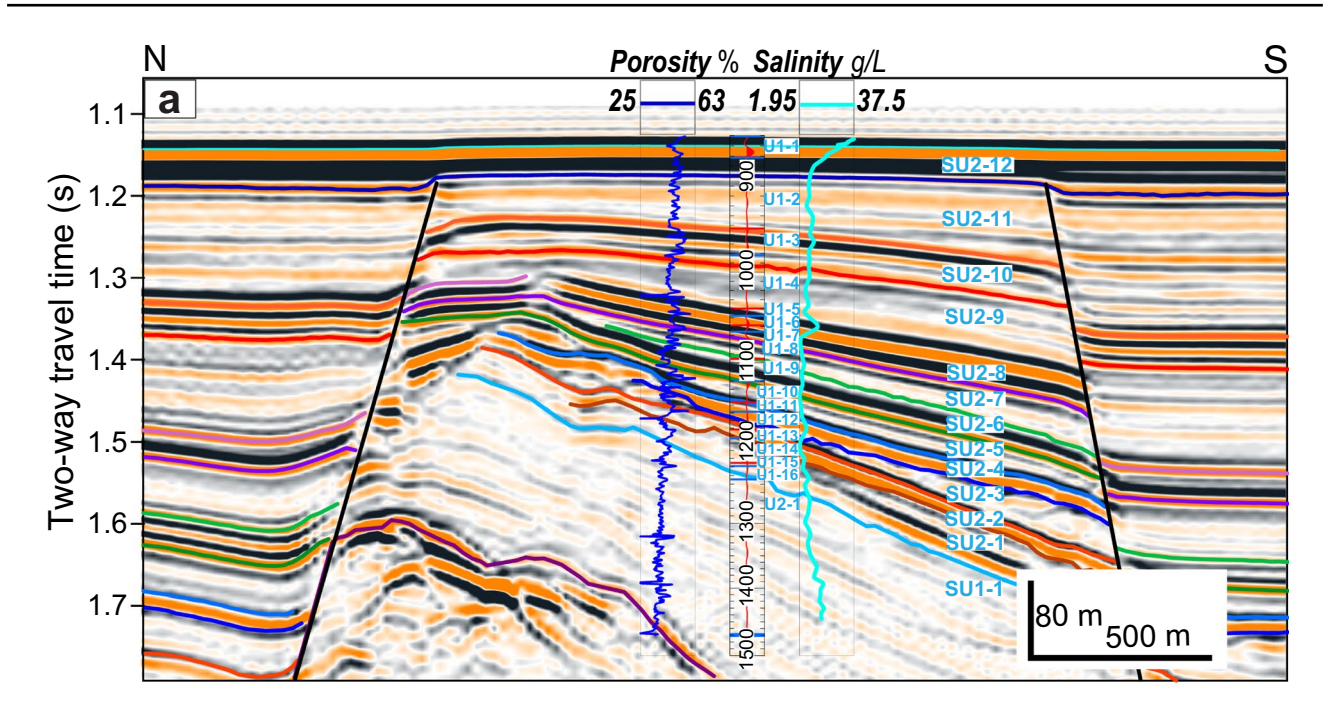
$$\alpha = c \cdot L^m$$

where c is a parameter characteristic for a geological medium $[L^{1-m}]$, L the flow distance [L], and m is the scaling exponent. These parameters have been quantified via the analysis of hundreds of data from unconsolidated sediments and consolidated rocks. The first kind of material has been considered in the present case, and an average flow distance of 1 km has been deemed appropriate for the groundwater flow taking place in a substantially vertical direction from the seafloor to the model bottom. The resulting longitudinal dispersivity is equal to 20 m and the transversal one is set to be a tenth of this value. A value of 1×10^{-9} m²/s was finally assigned to the molecular diffusion coefficient.

Initial and boundary conditions

The GOC has gone through a series of cycles characterized by lower sea levels fostering the entry and permanence of freshwater in the basin during glacial periods, alternating with interglacial stages marked by saltwater occurrence caused by the sea-level rise. To include these processes in the model, the cycles were reproduced starting from 800 ka, up to present-day conditions. Depending on the cycle under simulation, seawater hydraulic head values described in Table 2 were set as a Dirichlet condition at the uppermost layer representing the seafloor. Saltwater concentration was set on this boundary during interglacial cycles, whereas a freshwater concentration





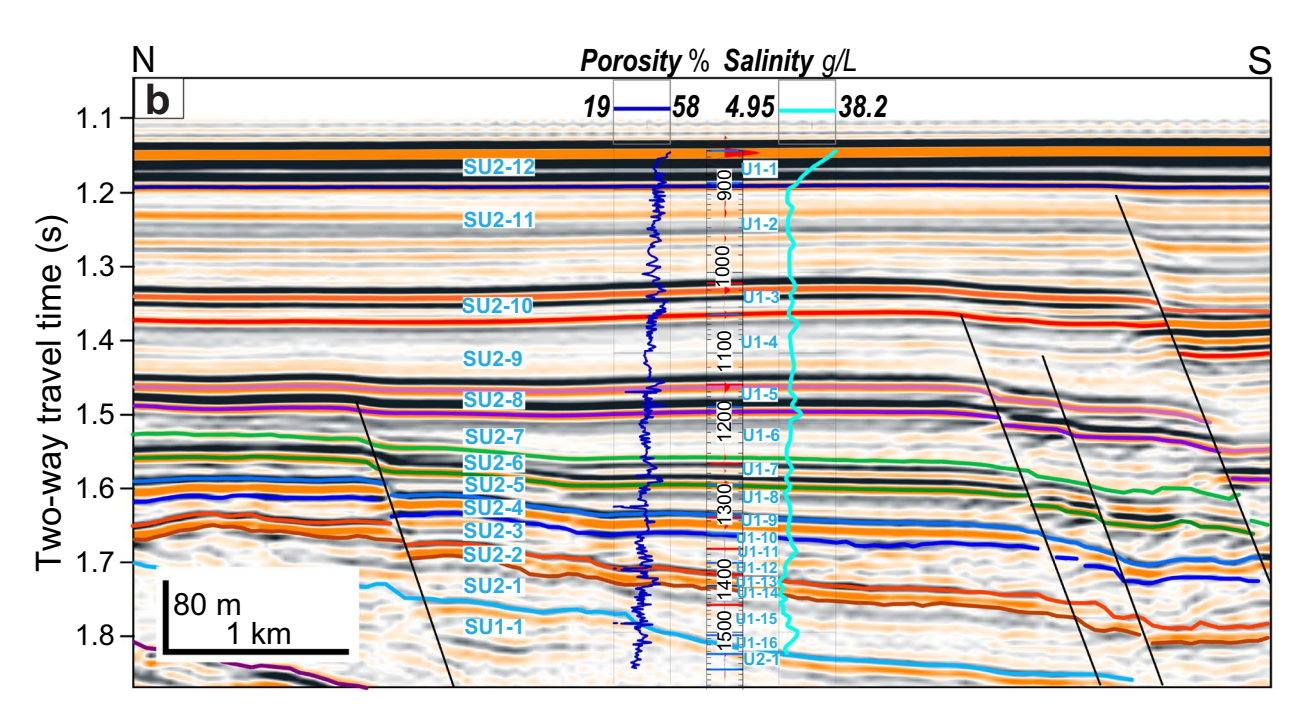


Fig. 6 Close-up interpreted seismic profiles superimposed with physical property data from the IODP sites: **a** M0078A, **b** M0079A, and **c** M0089A. The curve on the left is total porosity which ranges from 19 to 63%. The curve on the right of the site pertains to salinity (1.95–37.5 in M0078A, 4.95–38.2 in site M0079A, 12.3–40.5 in site M0089A). Seismic units (SU2-1 to SU2-12 and SU1-1) and

lithologic units (U1-1 to U1-16 and U2-1) are marked by red and blue lines, respectively, on the depth track (McNeill et al. 2019a, b). Green shading represents intervals with strong freshened water. In M0080A, the lowest salinity sediment intervals include SU2-5 and the lower part of SU2-6 in U1-3 and U1-4

was assigned during glacial periods (Table 2). No-flow conditions were assigned to the aquifer bottom. A freshwater initial condition was set in the whole domain for the first cycle, while model calculated concentrations obtained at the end of each cycle became the initial conditions for the subsequent one.



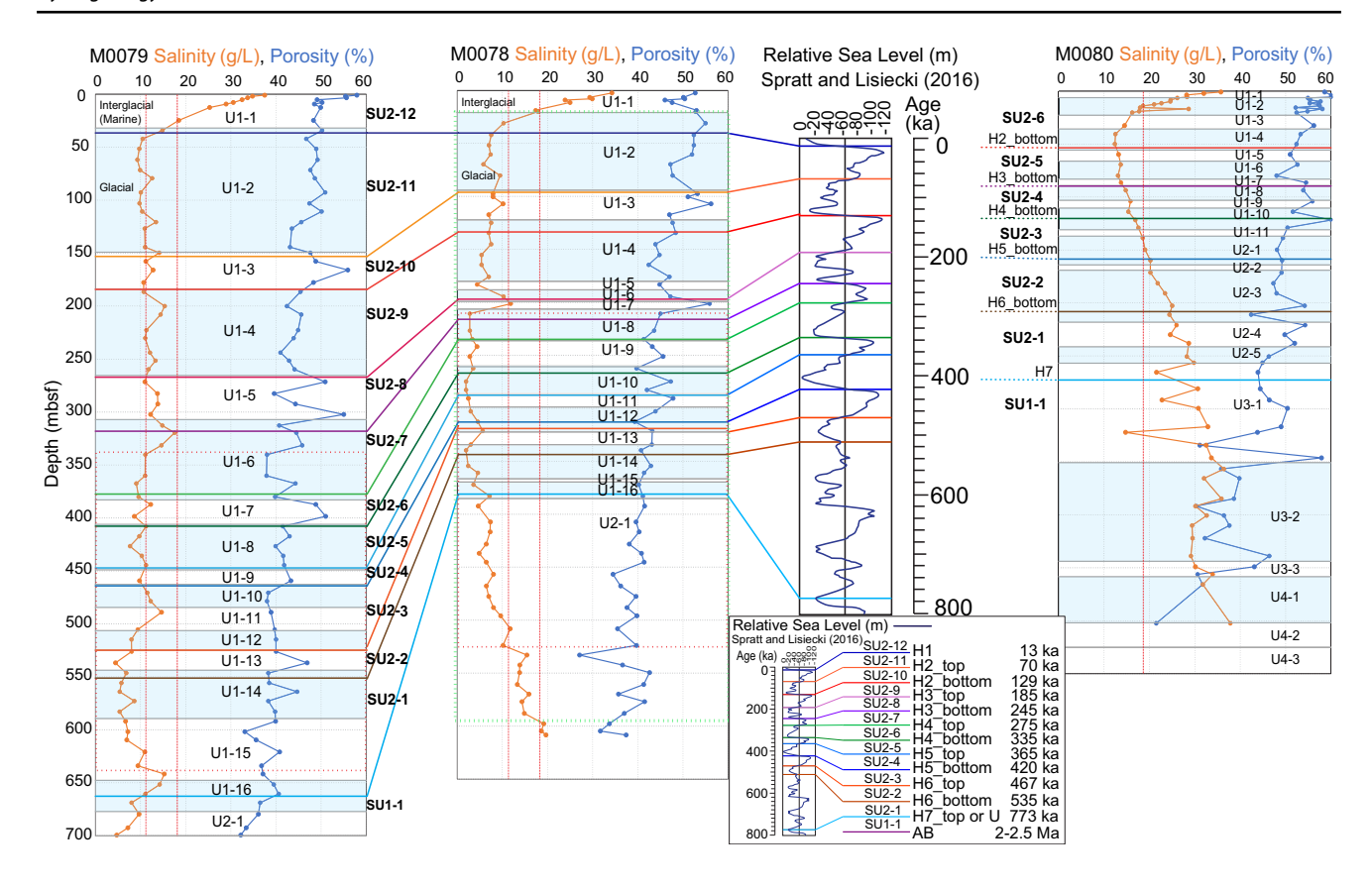


Fig. 7 Correlation of total porosity with salinity, plotted alongside seismic unit boundaries (H1–H7, colored lines) and lithologic units (*gray lines*). Red Lines represent salinity thresholds at 12 and 18.

Salinity in M0079A cores exceeds that in M0078A cores. Blue bands represent glacial intervals, while white bands indicate the interglacial periods

Results

Seismic stratigraphy

Thirteen seismic horizons (Fig. 5), including the top of the acoustic basement, were mapped and interpreted. On the basis of the nannofossils and foraminifera assemblages of core samples from the IODP site 381 sites (McNeill et al. 2019b), these horizons are dated between ca. 770 ka (H7) and 13 ka (H1) (Fig. 5). On seismic profiles, they are characterized by laterally continuous, low- to highamplitude reflections (Fig. 5). The seismic units defined by these horizons are referred to as SU1-1 and SU2-1 through SU2-12, from oldest to youngest (Fig. 5). H7 marks a significant unconformity or seismic unit boundary separating alternating, well-stratified, low- to high-amplitude seismic reflections above (seismic units SU2-1 to SU2-12) from discontinuous, low-amplitude seismic reflections below (SU1-1; Fig. 5). H7 also corresponds to the boundary between IODP lithostratigraphic units 1 and 2 (Fig. 3; McNeill et al. 2019a). The change in reflection pattern from SU1 to SU2 denotes a change in the depositional regime or environment.

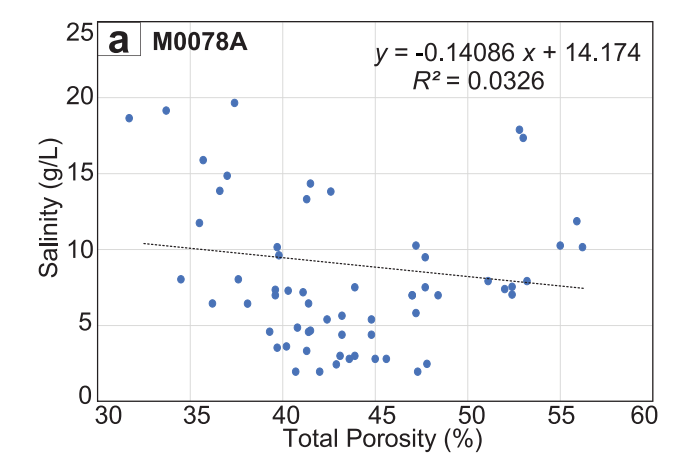
Seismic to well correlation at M0079A show that the seismic units generally correlate well with lithological subunits (Fig. 6). This correlation confirms that seismic units with odd numbers (SU2-5 to SU2-11) correspond to glacial periods, while those with even numbers (SU2-4 to SU2-12) represent interglacial periods (Figs. 5 and 6). Seismic units deposited during interglacial periods are characterized by continuous high-amplitude reflections, while those from glacial periods exhibit low-amplitude continuous reflections (Figs. 5 and 6).

The sedimentary strata in the central subbasin are intersected by numerous N- and S-dipping normal faults (Figs. 3 and 5); some extend into the seafloor, indicating recent activity. However, strata imaged at the IODP drill sites are not affected by faults and are nearly flat (Figs. 5 and 6). Seismic evidence of vertical and lateral fluid flow structures (e.g., pockmarks; seismic chimneys/pipes; bright spots) are absent on the seafloor and in the subsurface strata in the central and eastern subbasins.

Offshore freshened groundwater distribution

Pore-water salinity measurements from the three sites of Expedition 381 confirm the presence of freshened





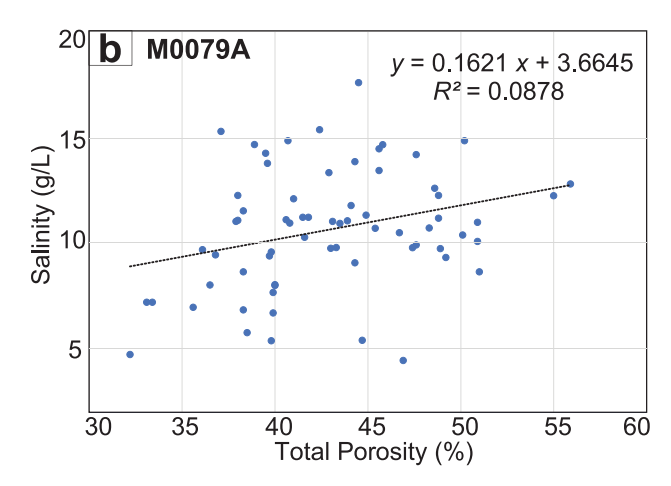
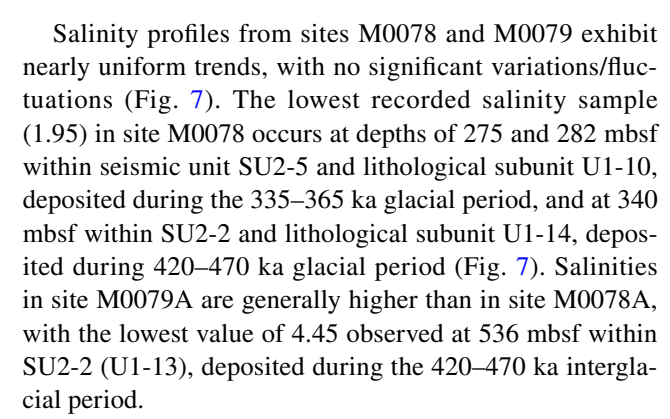


Fig. 8 Scatter plots of salinity (< 20) versus total porosity from IODP sites: **a** M0078A (R^2 <0.033), **b** M0078A (R^2 <0.102), and **c** M0080A (R^2 <0.088), indicating no correlation in the core measurements

groundwater (Fig. 7). Salinity values decrease sharply from over 38 g/L (or psu—practical salinity unit of seawater, or 38 g/kg, which is equal to 38 ppt—parts per thousand or ‰vol) to below 20 g/L (brackish water) at depths from 0 to 15–20m below seafloor (mbsf) (Fig. 7). Salinity values remain below 18 down to ca. 600 mbsf in site M0078A and ca. 700 mbsf in M0079A, corresponding to the seismic units SU1-1 through SU2-12. The lowest salinity values, indicating freshened water (< 5 in M0078A and < 13 in M0079A), occur in the central subbasin, specifically within the interval spanning from SU2-1 to SU2-7 (Fig. 7).

In the eastern subbasin, the brackish interstitial water with salinities ranging from 18 to 12 is predominantly confined to the upper 150 mbsf, situated between seismic units SU2-3 and SU2-6, except for a low salinity measurement at 325 mbsf (Fig. 7). Similar to M0078A and M0079A, salinity values in site M0080A decrease from 38 to below 20 at ca. 20 mbsf. The lowest recorded salinity, 12.3, was measured within seismic unit SU2-6 (Fig. 7).



Total porosities in sites M0078A and M0079A decrease abruptly from 60% to below 50% at depths of 15 to 20 mbsf (Fig. 7). Similar trends are observed in site M0080A, where total porosity values drop from 60% below 50% ca. 20 mbsf. Total porosities are generally higher in interglacial periods (ca. 50% on average) compared to glacial intervals (ca. 45% on average; Fig. 7). Overall, total porosities decrease with depth because of compaction. Scatter plots of salinity (< 20) versus total porosity in the three sites show no correlation, illustrating that salinity is independent of total porosity (Fig. 8).

The estimated volume of freshened water, calculated using seismic unit isopachs and mean total porosities derived from core petrophysical data, is 239.7 km³ in the central GOC and 11.3 km³ in the Alkyonides Gulf (Tables S2 and S3 of the ESM). Summing these volumes together, it is estimated that the mapped region contains at least 250 km³ of OFG (Tables S2 and S3 of the ESM).

3D stochastic modeling of petrophysical properties

The modelled total porosity and salinity volumes in 3D reveal the vertical and lateral distribution of total porosity and salinity in the stratigraphically mapped areas in the central and eastern subbasins (Fig. 9a–d). The total porosities and salinities in the study area range from 35 to 60% and 2.5 to 35, respectively (Fig. 9a–d). Salinities and total porosities are relatively higher in the uppermost sediments. Moreover, total porosities gradually decrease with depth, while salinities do not display any clear trends with depth.

A 3D volume rendering of the modeled salinity in the central subbasin (values between 2.5 and 5; Fig. 9e) and in the eastern subbasin (between 12.5 and 15; Fig. 9f) show the widespread occurrence of freshened groundwater throughout the gulf. The modelled 2D profiles traversing sites M0079A and M0078A (Fig. 10a, b) demonstrate that the total porosity of the individual seismic units is laterally continuous, with minimal heterogeneity. In contrast, total porosities exhibit vertical variations, showing an overall decreasing trend with depth. Similarly, the modelled data indicate that the seismic units consist of laterally continuous layers; however,



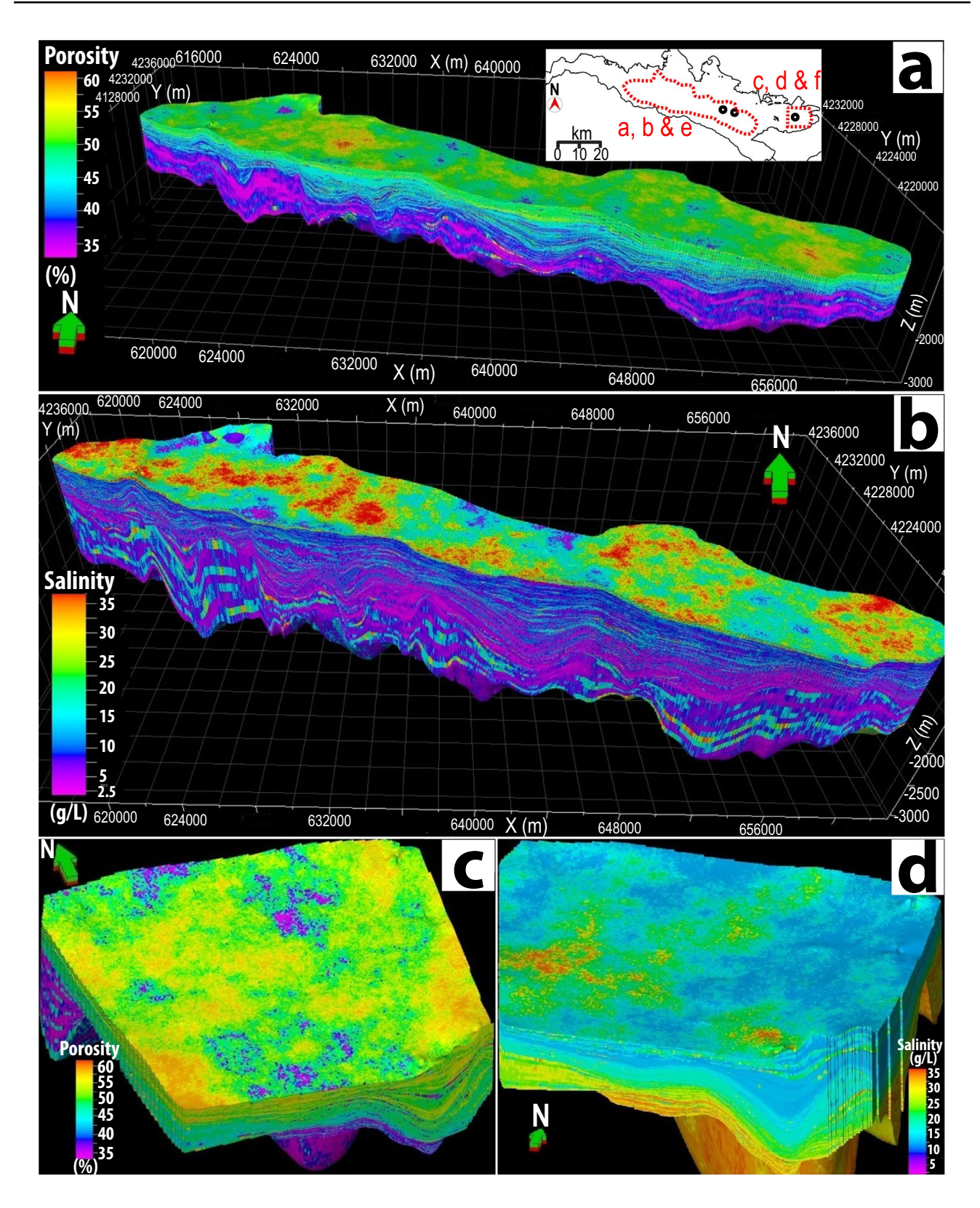


Fig. 9 3D models of **a** total porosity, **b** salinity for the central region (M0078A and M0079A), **c** total porosity, and **d** salinity for the eastern gulf (M0080A). Panels **e-f** illustrate 3D lateral and vertical distribution of low salinity in the central (2.5–5) and eastern basins

(12.5–15), respectively, highlighting the extent of freshened groundwater. Areal limits of the geological models in the central and eastern gulf regions are limited by the red polygons on the index map. For the scale of ${\bf c}$ and ${\bf d}$ please refer to part ${\bf f}$



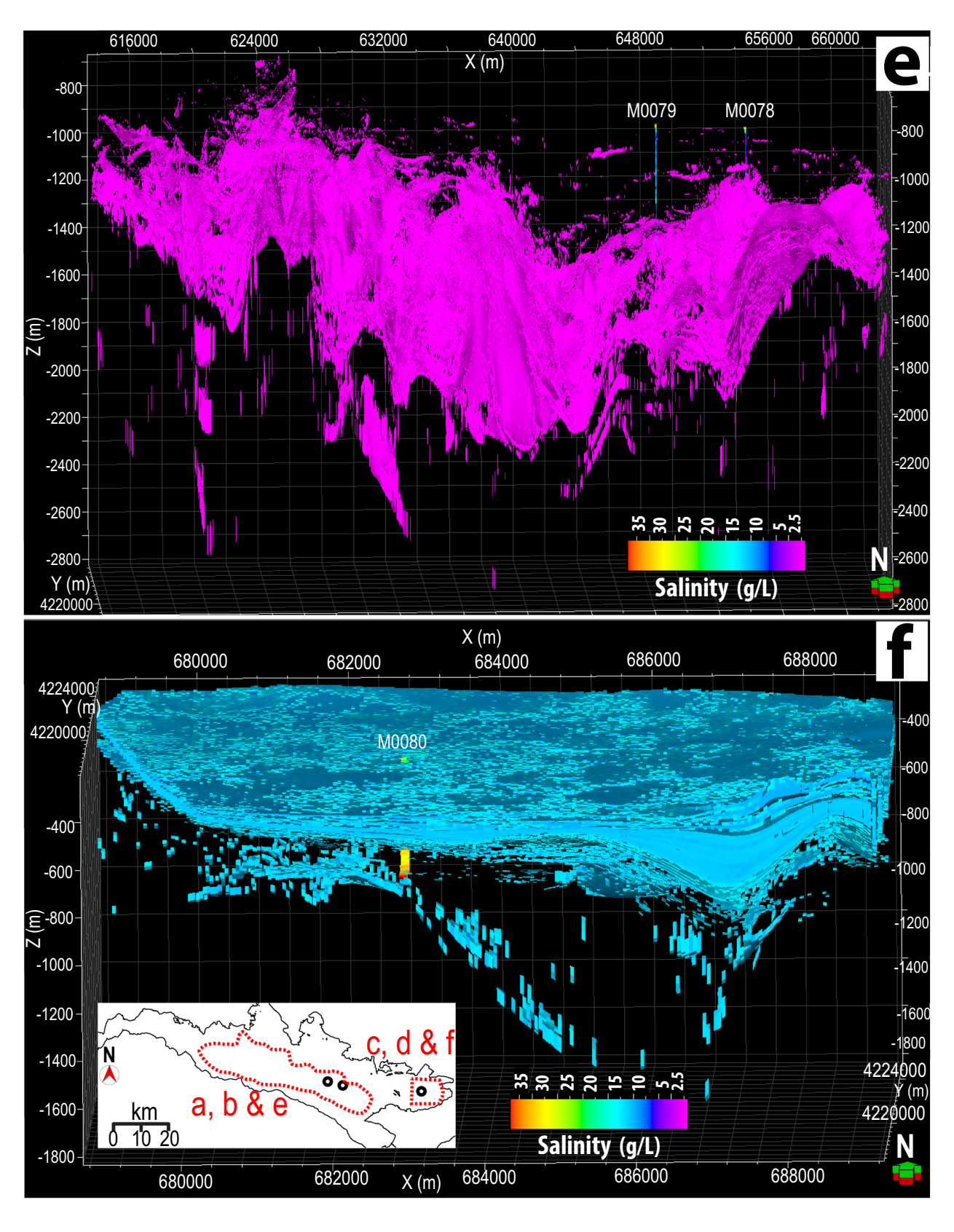


Fig. 9 (continued)



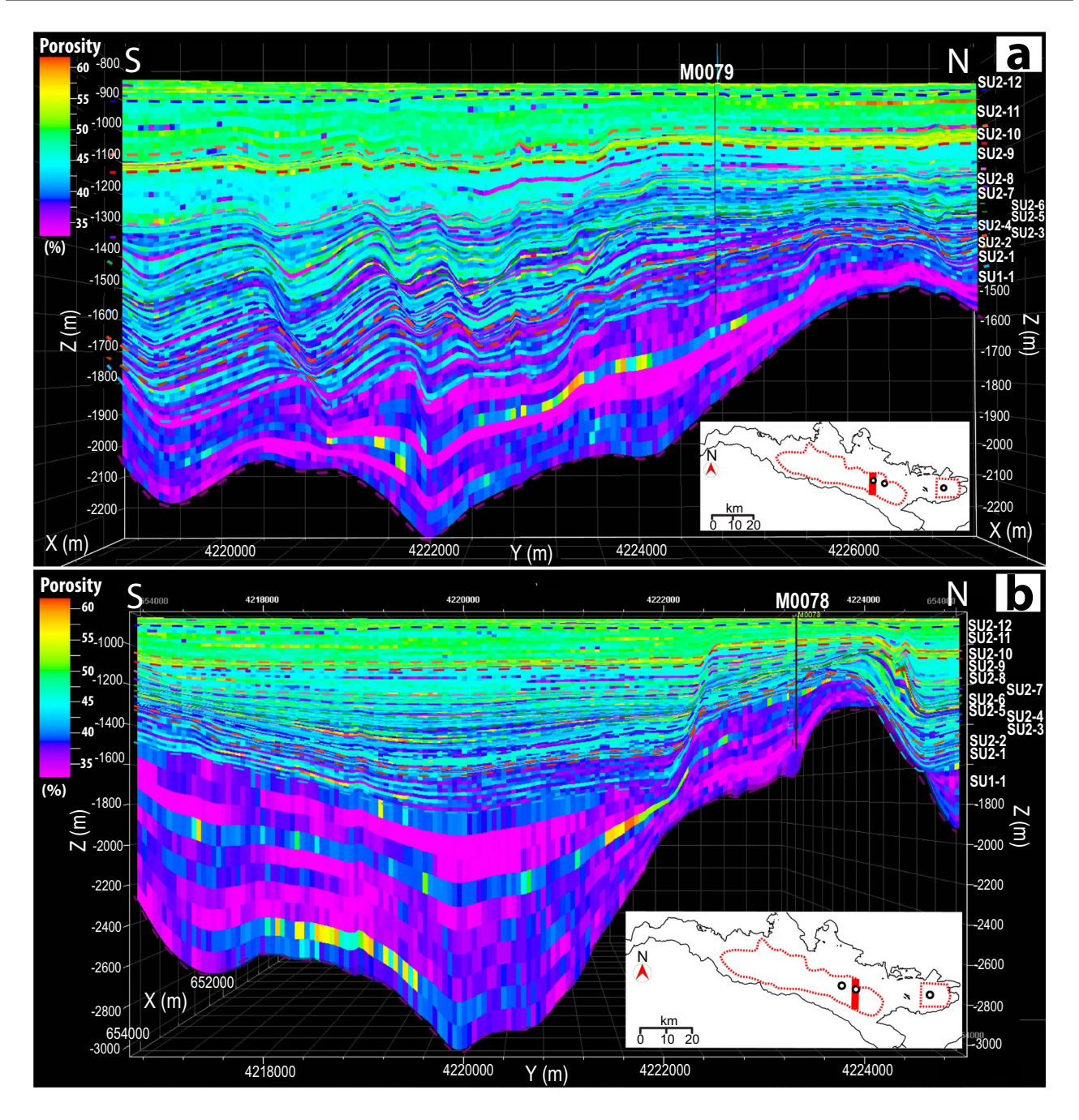


Fig. 10 2D cross-sections of total porosity and salinity models along $\bf a, c$ M0078A and $\bf b, d$ M0079A. Panels $(\bf e-\bf k)$ show low salinity (< 8 g/L) intervals in seismic units SU2-6 to SU1-1, occurring at

depths below 1000 m. The locations of sections crossing M0078 and M0079 wells are shown on the index maps with red bold lines

unlike total porosity, salinity profiles do not display distinct vertical trends within seismic units (Fig. 10c, d). Seismic units with the lowest salinities (< 7.5) in M0078A include SU2-6 (Fig. 10e), SU2-5 (Fig. 10f), SU2-4 (Fig. 10g), SU2-3 (Fig. 10h), SU2-2 (Fig. 10i), SU2-1 (Fig. 10j) and SU1-1 (Fig. 10k).

Vertical diffusive salt transport times

The calculated vertical diffusive salt transport times of Cl⁻ ion range from 69.2–531.9 ka in the glacial units and 12.2–139.9 ka in the interglacial units (Table 1). In SU2-3, which represents a mixed environment of both glacial and



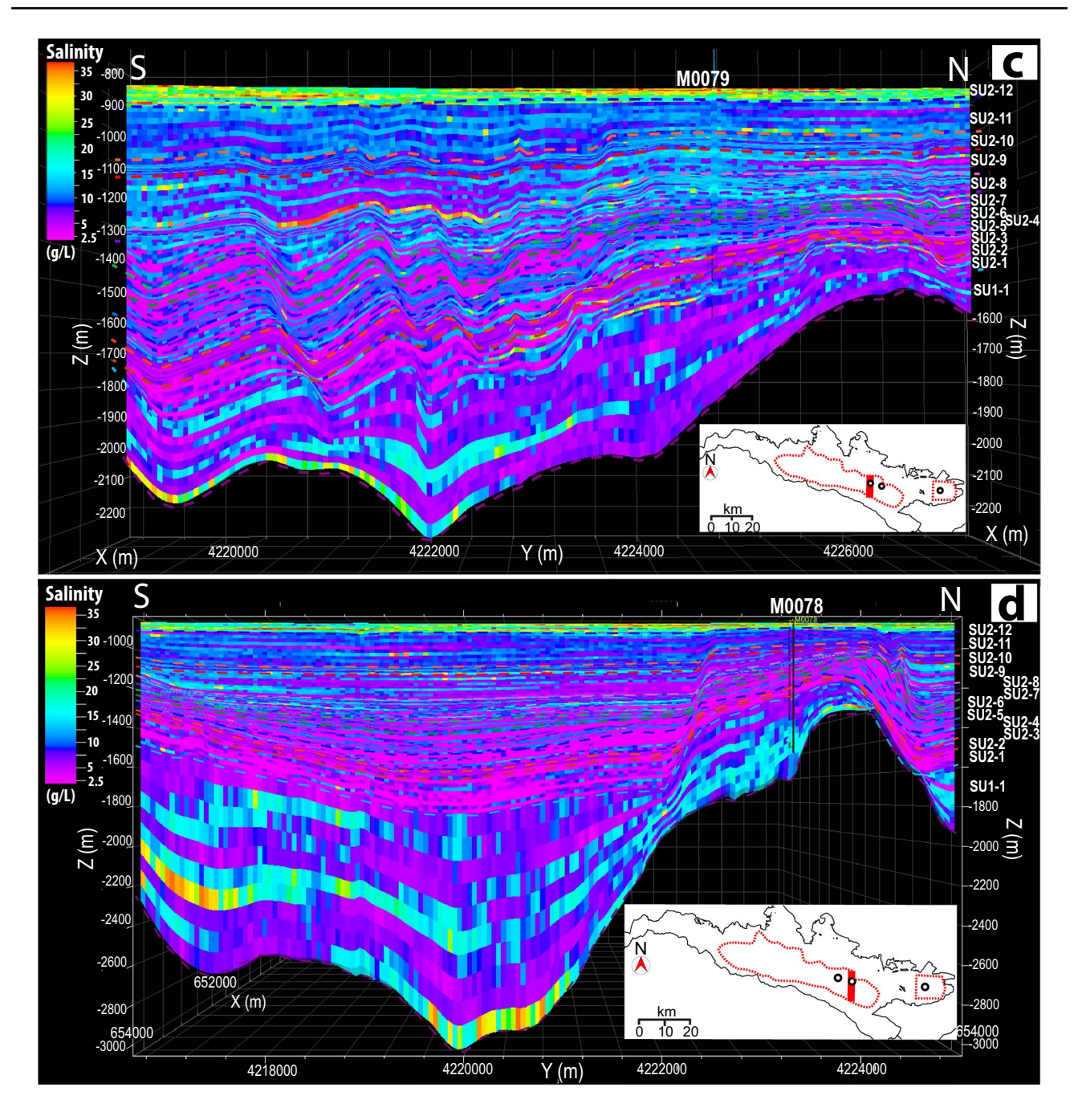


Fig. 10 (continued)

interglacial deposits, the diffusive salt transport time is 175.8 ka, while in SU1-1, it is 5470.3 ka. Diffusive salt transport times are generally greater in glacial intervals (even-numbered units, shown in bold text in Table 1), because of their greater unit thicknesses and lower hydraulic conductivities.

Conversely, vertical diffusive salt transport times in interglacial intervals (odd-numbered units) are lower, reflecting their lower thickness and higher hydraulic conductivities. Some interglacial units exhibit low salinity values (< 12, indicated in red in Table 1), with the lowest mean salinity observed in SU2-2. In this unit, the diffusive salt transport times are typically shorter (almost equal only in SU2-2) than the sedimentation time for these units.

Groundwater model results

Scatter graphs shown in Fig. 11a, b compare observed concentration data at various depths in site M0079 with concentrations



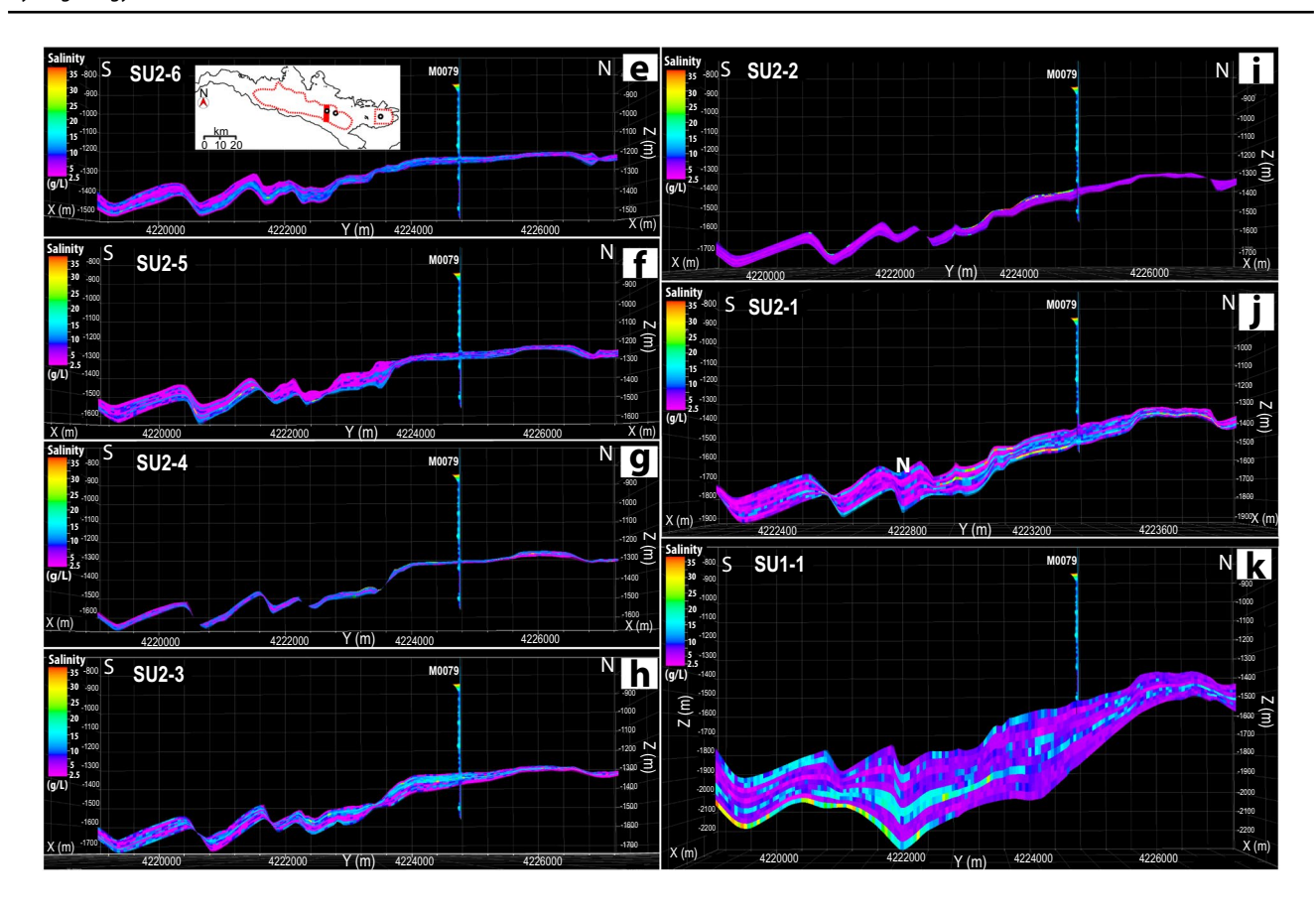


Fig. 10 (continued)

calculated by the groundwater model, along the corresponding vertical profile at the end of the time cycles (present-day conditions). The first scatter plot (Fig. 11a), derived from the simulations performed with the lowest distribution of K values, exhibit a correlation of $R^2 = 0.67$ with the observed data. This setup affects both groundwater flow and salt transport in a way that calculated concentrations appear to be confined to an area very close to the seafloor with respect to the observed one. The K distribution marked by the highest values, on the other hand, allows for better salt spreading, ensuring the presence of concentration values at greater depths (Fig. 11b). Therefore, the K values in the upper limit of the estimated variation range better reflects the field measurements ($R^2 = 0.89$). Finally, Fig. 11c shows the 2D spatial configuration of groundwater salinity, obtained with the higher K values, at the end of the sea level cycles simulation (present-day condition).

Discussion

Characteristics of OFG in the Gulf of Corinth

The total estimated volume of the OFG in the studied region of the GOC is 250 km³. With the GOC coastline

stretching ca. 410 km, this corresponds to a volume of 1.6 km³/km. This value is comparable to the other regions, such as 1.22–2.96 km³/km in the Canterbury Bight, New Zealand (Micallef et al. 2020), 1.6–1.8 km³/km offshore of New England (Cohen et al. 2010), and 1.0 km³/km offshore Jakarta (Post et al. 2013). Furthermore, the OFG in the GOC is one of the shallowest (ca. 20 mbsf) freshened water bodies below the seafloor documented globally (Micallef et al. 2021), and one of the thickest (ca. 1850 m). Similar thicknesses of sediment bodies bearing freshened water (ca. 1600 m) have been reported in Gippsland, Australia (Varma and Michael 2012).

From a hydrogeological perspective, the OFG in the GOC represent a significant freshwater resource. Considering Greece's annual groundwater consumption of 3.6 km³ (EASAC 2006), the OFG could potentially supply freshwater for ca. 70 years under current demands, assuming that the OFG is entirely fresh and no treatment is required.

Possible emplacement mechanisms and flow pathways for the OFG

The freshening of pore water in the GOC may be a result of several mechanisms, as outlined in the introduction. Among



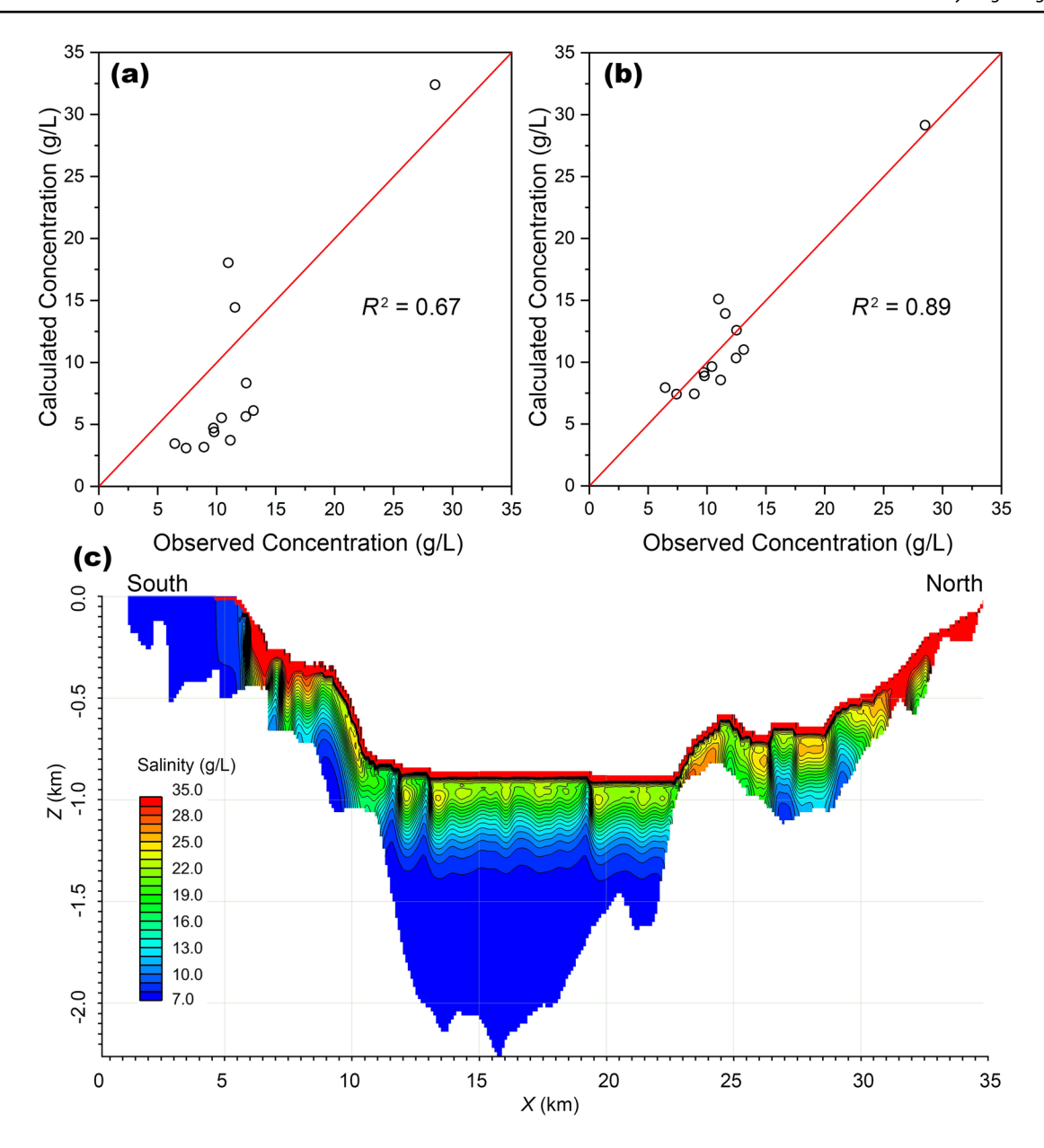


Fig. 11 Scatter plots of observed versus calculated salinity concentrations for **a** lowest and **b** highest hydraulic conductivity distribution. **c** Present-day 2D spatial distribution of groundwater salinity obtained with the parameter setup with the maximum limit of hydraulic con-

ductivities that are calculated in lithologies from the total porosities and D_{10} of grain size (point on the grain size distribution curve below which 10% of the particles fall). D_{10} is used 0.4 and 1 μ m for $\bf a$ and $\bf b$, respectively (Kang et al. 2022)

these, the most plausible explanation is meteoric recharge during glacial periods when the GOC became a lake disconnected from the open oceans (e.g., McNeill et al. 2019a, b). Under these circumstances, large volumes of fresh groundwater volumes may have been recharged through rainfall infiltration into the lake itself and from land because of higher hydraulic heads and steeper hydraulic gradients (Person et al. 2003; Cohen et al. 2010; Micallef et al. 2020). This hypothesis is further supported by 2D groundwater

modelling, which indicates that the freshened water in the deep basin is a relict from these lowstand periods, with no evidence of modern recharge. Furthermore, the absence of modern recharge is corroborated by seismic reflection data, which show no significant upward fluid migration in the deeper basinal areas (Figs. 3, 5 and 6).

Alternative mechanisms, such as post sedimentary alteration (diagenesis), gas hydrate dissociation, and the intrusion of modern meteoric water from coastal aquifers were



also considered. However, these are unlikely contributors in the GOC. Post sedimentary alteration can lead to release of freshwater and the formation of freshened water fronts in deeply buried marine sediments or in high pressure and temperature conditions in convergent margins (Micallef et al. 2020). Diagenesis of minerals such as silica (from Opal A to Opal CT) gypsum (dehydration to anhydrate), and clay (transformation of smectite to illite) are responsible for pore-water freshening in marine sediments (Micallef et al. 2020 and references therein). However, the influence of diagenesis on the formation of OFG can be ruled out in the study area because diagenetic minerals such as clays and zeolites are extremely low or absent in the sediments recovered (McNeill et al. 2019b), suggesting that smectite-illite is likely a small player in freshwater production in the subsurface sediments here. Freshening of pore waters in marine settings has also been reported in association with dissociating gas hydrate deposits (Hesse 2003; Moore et al. 2001), but neither seismic profiles nor sediment records show evidence of the presence of gas hydrates at the GOC sites. The intrusion of modern meteoric water from coastal aquifers may also cause elevated freshened waters in the subseafloor strata (Michael et al. 2016). However, any potential impact of modern recharge is likely to be small and restricted to the coastal areas, as documented by previous studies on the southern coast of the GOC where active groundwater discharge has been observed (Christodoulou et al. 2003; See Fig. 1). The IODP drilled sites are located in deep water depths of 850 m in the central subbasin and 350 m in the eastern subbasin, far away from the onshore aquifers, thus making this hypothesis unlikely. Additionally, the modelling results suggest that the freshened water in the deep basin is a relict from past lowstand periods, further supporting the idea that no modern recharge is occurring in these areas.

The process of vertical diffusion has played a critical role in the homogenization of salinity profiles across glacial and interglacial units. Glacial units exhibit significantly greater sedimentary thicknesses than interglacial units, resulting in longer vertical diffusion times owing to their lower hydraulic conductivities. The mean salinity values of some interglacial units (e.g., SU2-10, 2–6, and 2–4; red values in Table 1) are low, with SU2-2 showing even lower salinities than the glacial units. Diffusion time estimates at drilling site M0079A range from 12.2 and 139.9 ka, matching or being shorter than the sedimentation time of these units, indicating that these layers were desalinized by vertical diffusion (Table 1).

The petrophysical properties of glacial sediments, including low total porosity and permeability but greater thickness, likely allowed them to retain significant water volumes, preventing rapid flushing. These freshwater-charged glacial intervals are considered unconfined aquifers, whereas some interglacial units such as SU2-2, exhibit even lower mean salinities than glacial units. Over time, vertical diffusion

between interglacial and glacial units (aquifer-aquitard) likely occurred following their burial.

Impact of geological structures on OFG distribution

Salinity profiles from sites M0078A and M0079A reveal homogeneous trends, lacking significant fluctuations across seismic and lithological units from glacial and interglacial periods. Pore-water samples indicate freshened water occurs in both interglacial and glacial sediments, likely homogenized through vertical diffusion (Fig. 7). The glacial lowstand units, with relatively high total porosity (ca. 35–50%) and ca. 2–7 times greater thickness than interglacial units, suggest a greater storage capacity. Consistent with lithology, seismic data also show increased sediment thicknesses during lowstands (Figs. S3 and S4 of the ESM), when the basin was likely a restricted lake, the groundwater recharged from 360°.

Overlying interglacial highstand units, though thinner, have sufficient permeability to allow vertical diffusion over time. Seismic data show no evidence of fluid flow structures, such as pockmarks, that would suggest significant vertical migration driving OFG (Figs. 5 and 6). Pore-water salinity and total porosity plots further support homogenization by vertical diffusion, showing no correlation between salinity and total porosity (Fig. 8). This contrasts with studies off New Jersey, where total porosity and salinity exhibit an inverse relationship because of the cemented horizons acting as permeability barriers (Lofi et al. 2013). In the GOC, such cemented horizons are absent; instead, transitions between glacial and interglacial units are marked by unconsolidated, laminated beds (McNeill et al. 2019a), which allow upward fluid migration.

Lateral and vertical variations in total porosity, and hence permeability, would influence the fluid flow paths in the basin. Modeled total porosity and salinity distributions across the GOC show minimal lateral variation, consistent with laterally extensive seismic units with no significant seismic facies changes (Fig. 10a-d). This observation suggests that internal fluid flow in the GOC is likely to be diffuse. The modeled total porosity decreases with depth because of compaction (Fig. 10a, b), while salinity exhibits minor vertical variations in the OFG bearing zone, indicating independence from lithology, total porosity, or burial depth. Notably, the lowest salinity is observed in an interglacial deposit (U1-13 in SU2-2) within M0079A, where glacial sediments are relatively thick. As already noted previously, this pattern can be explained by homogenization by freshwaters through vertical diffusion between sedimentary layers deposited during glacial/interglacial cycles.

Extremely high salinities (up to 40) likely due to seawater mixing in recent marine sediments (Fig. 10c, d), occur



in the upper ca. 20 mbsf. The southern central subbasin, a major depocenter for glacial and interglacial seismic units (Fig. 5a), suggests tectonic activity along the southern boundary fault since the gulf's formation. While faults in deeper GOC sediments (Figs. 3 and 5) could enhance vertical permeability and fluid leakage, seismic reflection data do not show evidence of acoustic anomalies associated with fluid migration (e.g., pockmarks associated with submarine groundwater discharge). Therefore, it is not expected that faults would act as fluid pathways or barriers in the study area, at least in the deeper basinal areas.

Overall, the findings from the GOC provide insights into the mechanisms controlling OFG emplacement and distribution in rift basins. The results are in line with global studies (e.g., Micallef et al. 2021; Sheng et al. 2023; Thomas et al. 2019) which emphasize the importance of glacial recharge and sedimentary processes. However, the specific characteristics of the GOC, such as its shallow depth, thick freshwater zone, and lack of cemented barriers, highlight its uniqueness among OFG systems.

Limitations and uncertainties in the approach

The analysis of the OFG system in the GOC includes methodological limitations and assumptions that introduce uncertainties and highlight areas for improvement:

- The estimation of the total OFG volume (250 km³) relies on interpolation and modelling based on the limited borehole data from IODP sites. The lack of direct sampling across the entire GOC basin may lead to an underestimation of the total OFG volume. Expanding sampling and incorporating new geophysical data would improve these estimates.
- 2. The 2D hydrological model assumes basin-wide homogeneity conditions for some forcings affecting the system. The simulations have not accounted for groundwater recharge fluctuations due to seasonal variations or tidal effects, which could influence saline-water intrusion. Some hydrodynamic and hydrodispersive parameters such as specific yield, specific storage and longitudinal dispersivity, were sourced from existing literature related to the various lithologies within the area, rather than through specific experimental testing. Including these aspects in the model could potentially enhance the accuracy of the outcomes.
- 3. Although this study suggests minimal modern recharge because of the depth of the drill sites, the potential influence of nearshore processes or seasonal variations in coastal aquifer discharge is not fully quantified. Monitoring modern groundwater fluxes using time-series data could clarify the role of active recharge mechanisms.

Conclusions

The spatial distribution, emplacement mechanisms, and geological controls of freshened groundwater in the rift basin of the GOC were investigated by integrating the 2D seismic reflection data, core physical properties, lithostratigraphy, and groundwater modelling. Salinity profiles from IODP Expedition 381 sites reveal significant freshening of pore waters, extending from ca. 20 mbsf to ca. 600-700 mbsf in the central subbasin and from ca. 15 to ca. 150 mbsf in the eastern subbasin of the Alkyonides Gulf. The freshwater is likely the result of recharge of meteoric water into the lake itself and from adjacent coastline during glacial periods. A 2D hydrogeological model of salinity changes over the past 800 ka supports this interpretation, suggesting that the OFG in the deep basin is a remnant from sealevel lowstands. The freshwater is stored in both interglacial and glacial sediments, with salinity variations independent of total porosity. This suggests that freshened water has been homogenized through diffusion across sediments deposited through successive glacial and interglacial cycles. Sediments deposited during glacial periods, with their considerable thickness and relatively high total porosity, likely had a greater capacity for freshwater storage. On the other hand, the overlying thin, saline marine units facilitated vertical freshwater penetration and homogenization over time. Seismic data reveal thick (up to 1840 m in the depocenter), laterally continuous sedimentary units that are estimated to contain 250 km³ of freshened water. Overall, this study documents the role of long-term sea-level fluctuations in groundwater freshening.

Supplementary Information The online version contains supplementary material available at https://doi.org/10.1007/s10040-025-02943-x.

Acknowledgements We used IHS Kingdom Suite© for seismic data interpretation and volumetric analysis, Petrel© for 3D petrophysical modelling and SEAWAT for hydrogeological modelling. We would like to thank Associate Editor Dr. Marwan Fahs and two anonymous reviewers for their constructive comments.

Author Contribution All authors contributed to the conceptualization, analysis and modelling, writing and revision process of this manuscript.

Funding Open Access funding provided by the University of Malta. S.H. was funded by the University of Malta on the basis of work on the project CA21112 Offshore freshened groundwater: an unconventional water resource in coastal regions? (OFF-SOURCE), supported by the COST (European Cooperation in Science and Technology). A.M. was supported by the David and Lucile Packard Foundation.

Data Availability Datasets used in this study are publicly available and can be excessed online at: https://www.marine-geo.org/tools/search/entry.php?id=EW0108#datasets https://iodp.pangaea.de/front_content.php?idcat=615.

Declarations

Ethics approval and consent to participate Not applicable.



Consent for publication Not applicable.

Competing interests The authors declare they have no known commercial, personal or other associations that might pose a conflict of interest in connection with the submitted material.

Open Access This article is licensed under a Creative Commons Attribution 4.0 International License, which permits use, sharing, adaptation, distribution and reproduction in any medium or format, as long as you give appropriate credit to the original author(s) and the source, provide a link to the Creative Commons licence, and indicate if changes were made. The images or other third party material in this article are included in the article's Creative Commons licence, unless indicated otherwise in a credit line to the material. If material is not included in the article's Creative Commons licence and your intended use is not permitted by statutory regulation or exceeds the permitted use, you will need to obtain permission directly from the copyright holder. To view a copy of this licence, visit http://creativecommons.org/licenses/by/4.0/.

References

- Bakken TH, Ruden F, Mangset LE (2012) Submarine groundwater: a new concept for the supply of drinking water. Water Resour Manage 26:1015–1026
- Bell RE, McNeill L, Bull JM, Henstock TJ (2008) Evolution of the offshore western Gulf of Corinth. Geol Soc Am Bull 120:156–178
- Bell RE, McNeill L, Bull JM, Henstock TJ, Collier REL, Leeder MR (2009) Fault architecture, basin structure and tectonic evolution of the Corinth rift, central Greece. Basin Res 21:824–855
- Bell RE, McNeill LC, Henstock TJ, Bull JM (2011) Comparing extension on multiple time and depth scales in the Corinth Rift, central Greece. Geophys J Int 186(2):463–470. https://doi.org/10.1111/j. 1365-246X.2011.05077.x
- Berndt C, Micallef A (2019) Could offshore groundwater rescue coastal cities? Nature 574(7776):36. https://doi.org/10.1038/d41586-019-02924-7
- Bertoni C, Lofi J, Micallef A, Moe H (2020) Seismic reflection methods in offshore groundwater research. Geosciences 10(8):299. https://doi.org/10.3390/geosciences10080299
- Bratton JF (2007) The importance of shallow confining units to submarine groundwater flow. IAHS Publ 312:28–34
- Brown KM, Saffer DM, Bekins BA (2001) Smectite diagenesis, porewater freshening, and fluid flow at the toe of the Nankai wedge. Earth Planet Sci Lett 194(1–2):97–109. https://doi.org/10.1016/ S0012-821X(01)00546-5
- Carman PC (1956) Flow of gases through porous media. Butterworths, London
- Chowdhury F, Gong J, Rau GC, Timms WA (2022) Multifactor analysis of specific storage estimates and implications for transient groundwater modelling. Hydrogeol J 30:2183–2204. https://doi.org/10.1007/s10040-022-02535-z
- Christodoulou D, Papatheodorou G, Ferentinos G, Masson M (2003) Active seepage in two contrasting pockmark fields in the Patras and Corinth gulfs, Greece. Geo-Mar Lett 23:194–199. https://doi.org/10.1007/s00367-003-0151-0
- Cohen D, Person M, Wang P, Gable CW, Hutchinson D, Marksamer A, et al (2010) Origin and extent of freshwater paleowaters on the Atlantic continental shelf, USA. Groundwater 48(1):143–158. https://doi.org/10.1111/j.1745-6584.2009.00627.x
- Davies CPN (1997) Hydrocarbon evolution of the Bredasdorp Basin, offshore South Africa: from source to reservoir. University of Stellenbosch, Stellenbosch, South Africa. PhD Thesis, 1123 pp

- De Biase M, Chidichimo F, Maiolo M, Micallef A (2021) The impact of predicted climate change on groundwater resources in a Mediterranean archipelago: a modelling study of the Maltese Islands. Water 13(21):3046. https://doi.org/10.3390/w13213046
- EASAC (2006) Groundwater in the Southern Member States of the European Union: an assessment of current knowledge and future prospects. Reports statements, Country report for Greece, European Aviation Safety Agency, Cologne, Germany, 37 pp
- EW0108 Cruise Scientists (2001) Preliminary cruise report of the EW0108 cruise: Kolpos Korinthiakos deep seismic imaging of active continental extension. R/V Maurice Ewing. LDEO, Columbia University, NY, 25 pp. https://www.marine-geo.org/tools/search/entry.php?id=EW0108#documents. Accessed August 2025
- Ferentinos G, Papatheodorou G, Collins MB (1988) Sediment transport processes on an active submarine fault escarpment: Gulf of Corinth, Greece. Mar Geol 83(1–4):43–61
- Ford M, Rohais S, Williams EA, Bourlange S, Jousselin D, Backert N, Malartre F (2013) Tectono-sedimentary evolution of the western Corinth rift (central Greece). Basin Res 25(1):3–25. https://doi.org/10.1111/j.1365-2117.2012.00550.x
- Gawthorpe RL, Andrews JE, Collier REL, Ford M, Henstra GA, Kranis H, Leeder MR, Muravchik M, Skourtsos E (2017) Building up or out? Disparate sequence architectures along an active rift margin: Corinth rift, Greece. Geology 45(12):1111–1114
- Gawthorpe RL, Leeder MR, Kranis H, Skourtsos E, Andrews JE, Henstra GA, Mack GH, Muravchik M, Turner JA, Stamatakis M (2018) Tectono-sedimentary evolution of the Plio-Pleistocene Corinth rift, Greece. Basin Res 30(3):448–479
- Gawthorpe RL, Fabregas N, Pechlivanidou S, Ford M, Collier REL, Carter GD, McNeill LC, Shillington DJ (2022) Late quaternary mud-dominated, basin-floor sedimentation of the Gulf of Corinth, Greece: implications for deep-water depositional processes and controls on syn-rift sedimentation. Basin Res 34(5):1567–1600
- Giurgea V, Rettenmaier D, Pizzino L, Unkel I, Hötzl H, Förster A, Quattrocchi F (2004) Preliminary hydrogeological interpretation of the Aigion area from the AIG10 borehole data. CR Geosci 336(4–5):467–475. https://doi.org/10.1016/j.crte.2003.12.012
- Groen J, Velstra J, Meesters A (2000) Salinization processes in pale-owaters in coastal sediments of Suriname: evidence from Δ37Cl analysis and diffusion modelling. J Hydrol 234(1–2):1–20. https://doi.org/10.1016/S0022-1694(00)00235-3
- Gustafson C, Key K, Evans RL (2019) Aquifer systems extending far onshore on the US Atlantic Margin. Sci Rep 9:8709
- Haroon A, Micallef A, Jegen M, Schwalenberg K, Karstens J, Berndt C, Garcia X, Kühn M, Rizzo E, Fusi NC, Ahaneku CV (2021) Electrical resistivity anomalies offshore a carbonate coastline: evidence for freshened groundwater? Geophys Res Lett 48(3):e2020GL091909
- Hathaway JC, Poag CW, Valentine PC, Manheim FT, Kohout FA, Bothner MH, Miller RE, Schultz DM, Sangrey DA (1979) US Geological Survey core drilling on the Atlantic Shelf: geologic data were obtained at drill-core sites along the eastern US continental shelf and slope. Science 206(4418):515–527
- Head M, Gibbard PL (2005) Early-middle Pleistocene transitions: an overview and recommendation for the defining boundary. Geol Soc London Spec Publ 247(1):1–18. https://doi.org/10.1144/gsl.sp.2005.247.01.01
- Hesse R (2003) Pore water anomalies of submarine gas-hydrate zones as tool to assess hydrate abundance and distribution in the subsurface: what have we learned in the past decade? Earth Sci Rev 61(1–2):149–179
- Hüpers A, Kopf AJ (2012) Effect of smectite dehydration on pore water geochemistry in the shallow subduction zone: an experimental approach. Geochem Geophys Geosyst. https://doi.org/ 10.1029/2012GC004212



- IODP Expedition 381 Scientists (2020) Corinth Active Rift development. International Ocean Discovery Program (IODP) 381, College Station, TX. https://iodp.pangaea.de/front_content.php?idcat=615. Accessed August 2025
- Kafetzidou A, Fatourou E, Panagiotopoulos K, Marret F, Kouli K (2023) Vegetation composition in a typical Mediterranean setting (Gulf of Corinth, Greece) during successive Quaternary climatic cycles. Quaternary 6(2):30
- Kang W, Li S, Gawthorpe R, Ford M, Collier R, Yu X, Janikian L, Nixon C, Sergiou S, Gillespie J, Pechlivanidou S, de Gelder G (2022) Grain-size analysis of the late pleistocene sediments in the corinth rift: insights into strait influenced hydrodynamics and provenance of an active rift basin. Geological Society, London, Special Publications, p 523. https://doi.org/10.1144/ SP523-2022-166
- Kooi H, Groen J (2001) Offshore continuation of coastal groundwater systems: predictions using sharp-interface approximations and variable-density flow modelling. J Hydrol 246(1–4):19–35
- Kozeny J (1927) Uber kapillare leitung des wassers im boden (On capillary conduction of water in the soil). Sitzungsberichte der Kaiserlichen Akademie der Wissenschaften. Proc Imperial Acad Sci 136(2a):271–306
- Langevin CD, Thorne DT Jr, Dausman AM, Sukop MC, Guo W (2008) SEAWAT Version 4: a computer program for simulation of multispecies solute and heat transport. US Geol Surv Techniques Methods. https://doi.org/10.3133/tm6A22
- Lemieux JM, Hassaoui J, Molson J, Therrien R, Therrien P, Chouteau M, Ouellet M (2015) Simulating the impact of climate change on the groundwater resources of the Magdalen Islands, Québec Canada. J Hydrol Reg Stud 3:400–423. https://doi.org/10.1016/j.ejrh.2015.02.011
- Lin Q, Wang J, Algeo TJ, Su P, Hu G (2016) Formation mechanism of authigenic gypsum in marine methane hydrate settings: evidence from the northern South China Sea. Deep Sea Res Part I 115:210–220
- Lipparini L, Chiacchieri D, Bencini R, Micallef A (2023) Extensive freshened groundwater resources emplaced during the Messinian sea-level drawdown in southern Sicily, Italy. Commun Earth Environ 4(1):430
- Lofi J, Inwood J, Proust JN, Monteverde DH, Loggia D, Basile C, Otsuka H, Hayashi T, Stadler S, Mottl MJ, Fehr A (2013) Freshwater and salt-water distribution in passive margin sediments: insights from Integrated Ocean Drilling Program Expedition 313 on the New Jersey Margin. Geosphere 9(4):1009–1024
- Loveless SE (2013) The hydrogeological structure of fault zones in poorly lithified sediment, Gulf of Corinth rift. PhD Thesis, University of East Anglia, UK, 236 pp. https://core.ac.uk/download/pdf/19905422.pdf. Accessed August 2025
- Lv M, Xu Z, Yang ZL, Lu H, Lv M (2021) A comprehensive review of specific yield in land surface and groundwater studies. J Adv Model Earth Syst 13:e2020MS002270. https://doi.org/10.1029/2020MS002270
- Lykousis V, Sakellariou D, Moretti I, Kaberi H (2007a) Late quaternary basin evolution of the Gulf of Corinth: sequence stratigraphy, sedimentation, fault–slip and subsidence rates. Tectonophysics 440(1–4):29–51
- Lykousis V, Sakellariou D, Rousakis G, Alexandri S, Kaberi H, Nomikou P, Georgiou P, Balas D (2007b) Sediment failure processes in active grabens: the western Gulf of Corinth (Greece). In: Lykousis V, Sakellariou D, Loca J (eds) Submarine mass movements and their Consequences. Adv Nat Technol Hazards Res 27:297–305
- Mahoney C, März C (2022) Tracing glacial-interglacial water mass changes in the Gulf of Corinth (IODP expedition 381) using

- iron-sulphur geochemistry and magnetic susceptibility. Mar Geol 448:106801
- Malinverno A, Kastner M, Torres ME, Wortmann UG (2008) Gas hydrate occurrence from pore water chlorinity and downhole logs in a transect across the northern Cascadia margin (integrated ocean drilling program expedition 311). J Geophys Res Solid Earth. https://doi.org/10.1029/2008JB005702
- McNeill LC, Cotterill CJ, Henstock TJ, Bull JM, Stefatos A, Collier RL, Papatheoderou G, Ferentinos G, Hicks SE (2005) Active faulting within the offshore western Gulf of Corinth, Greece: implications for models of continental rift deformation. Geology 33(4):241–244
- McNeill LC, Shillington DJ, Carter GDO, the Expedition 381 Participants (2019a) Corinth Active Rift Development. Proceedings of the International Ocean Discovery Program, College Station, TX. https://doi.org/10.14379/iodp.proc.381.2019
- McNeill LC, Shillington DJ, Carter GD, Everest JD, Gawthorpe RL, Miller C, Phillips MP, Collier REL, Cvetkoska A, De Gelder G, Diz P (2019b) High-resolution record reveals climate-driven environmental and sedimentary changes in an active rift. Sci Rep 9(1):3116
- Micallef A (2020) Global database of offshore freshened groundwater records. Creative Commons Attribution 4.0 International. https://doi. org/10.5281/zenodo.4247833
- Micallef A, Haroon A, Person MA, Weymer B, Jegen MD, Schwalenberg K, Faghih Z, Duan S, Cohen D, Mountjoy JJ, Woelz S (2019) 3D characterisation of an offshore freshened groundwater system in a passive siliciclastic margin: Canterbury Bight, New Zealand. In: AGU Fall Meeting Abstracts, vol 2019, San Francisco, Dec 2019, pp H53I-1879
- Micallef A, Person M, Haroon A, Weymer BA, Jegen M, Schwalenberg
 K, Faghih Z, Duan S, Cohen D, Mountjoy JJ, Woelz S (2020)
 3D characterisation and quantification of an offshore freshened groundwater system in the Canterbury Bight. Nat Commun 11(1):1372
- Micallef A, Person M, Berndt C, Bertoni C, Cohen D, Dugan B, Evans R, Haroon A, Hensen C, Jegen M, Key K (2021) Offshore freshened groundwater in continental margins. Rev Geophys 59(1):e2020RG000706
- Michael HA, Scott KC, Koneshloo M, Yu X, Khan MR, Li K (2016) Geologic influence on groundwater salinity drives large seawater circulation through the continental shelf. Geophys Res Lett 43(20):10–782
- Moore GF, Taira A, Klaus A (2001) Initial report leg 190. In: Proceedings of the Ocean Drilling Program, College Station, TX, June 2001
- Moore JC, Saffer D (2001) Updip limit of the seismogenic zone beneath the accretionary prism of southwest Japan: an effect of diagenetic to low-grade metamorphic processes and increasing effective stress. Geology 29(2):183–186
- Morgan LK, Werner AD, Patterson AE (2018) A conceptual study of offshore fresh groundwater behaviour in the Perth Basin (Australia): modern salinity trends in a prehistoric context. J Hydrol Reg Stud 19:318–334
- Nixon CW, McNeill LC, Bull JM, Bell RE, Gawthorpe RL, Henstock TJ, Christodoulou D, Ford M, Taylor B, Sakellariou D, Ferentinos G (2016) Rapid spatiotemporal variations in rift structure during development of the Corinth Rift, central Greece. Tectonics 35(5):1225–1248
- Perissoratis C, Piper DJW, Lykousis V (2000) Alternating marine and lacustrine sedimentation during late quaternary in the Gulf of Corinth rift basin, central Greece. Mar Geol 167(3–4):391–411
- Person MA, Micallef A (2022) Offshore freshened groundwater in continental shelf environments. In: Qadir M, Smakhtin V, Koo-Oshima S, Guenther E (eds) Unconventional water resources. Springer, Cham. https://doi.org/10.1007/978-3-030-90146-2_5



- Person M, Dugan B, Swenson JB, Urbano L, Stott C, Taylor J, Willett M (2003) Pleistocene hydrogeology of the Atlantic continental shelf, New England. Geol Soc Am Bull 115(11):1324–1343
- Person MA, Bense V, Cohen D, Banerjee A (2012) Models of ice-sheet hydrogeologic interactions: a review. Geofluids 12(1):58–78
- Post VE, Groen J, Kooi H, Person M, Ge S, Edmunds WM (2013) Offshore fresh groundwater reserves as a global phenomenon. Nature 504(7478):71–78
- Poulos SE, Collins MB, Pattiaratchi C, Cramp A, Gull W, Tsimplis M, Papatheodorou G (1996) Oceanography and sedimentation in the semi-enclosed, deep-water Gulf of Corinth (Greece). Mar Geol 138:313–314. https://doi.org/10.1016/0025-3227(96)00028-X
- Rohais S, Eschard R, Guillocheau F (2008) Depositional model and stratigraphic architecture of rift climax Gilbert-type fan deltas (Gulf of Corinth, Greece). Sed Geol 210(3–4):132–145. https:// doi.org/10.1016/j.sedgeo.2008.08.001
- Sachpazi M, Clément C, Laigle M, Hirn A, Roussos N (2003) Rift structure, evolution, and earthquakes in the Gulf of Corinth, from reflection seismic images. Earth Planet Sci Lett 216(3):243–257
- Schulze-Makuch D (2005) Longitudinal dispersivity data and implications for scaling behavior. Ground Water 43(3):443–456. https://doi.org/10.1111/j.1745-6584.2005.0051.x
- Sergiou S, Beckers A, Geraga M, Papatheodorou G, Papaefthymiou H (2016) Recent sedimentary processes in the western Gulf of Corinth, Greece: seismic and aseismic turbidites. Bull Geol Soc Greece 50:383–391
- Sheng S, Chen Q, Li J, Chen H (2023) The improved reservoir module of SWAT model with a dispatch function and its application on assessing the impact of climate change and human activities on runoff change. Water 15(14):2620

- Spratt RM, Lisiecki LE (2016) A late Pleistocene sea-level stack. Clim Past 12:1079–1092. https://doi.org/10.5194/cp-12-1079-2016
- Taylor B, Weiss JR, Goodliffe AM, Sachpazi M, Laigle M, Hirn A (2011) The structures, stratigraphy and evolution of the Gulf of Corinth rift, Greece. Geophys J Int 185(3):1189–1219
- Thomas AT, Reiche S, Riedel M, Clauser C (2019) The fate of submarine fresh groundwater reservoirs at the New Jersey Shelf, USA. Hydrogeol J 27(7):2673–2694
- Uchupi E, Driscoll N, Ballard RD, Bolmer ST (2001) Drainage of late Wisconsin glacial lakes and the morphology and late Quaternary stratigraphy of the New Jersey–southern New England continental shelf and slope. Mar Geol 172(1–2):117–145
- Varma S, Michael K (2012) Impact of multi-purpose aquifer utilisation on a variable-density groundwater flow system in the Gippsland Basin, Australia. Hydrogeol J 20(1):119
- Weymer BA, Wernette PA, Everett ME, Pondthai P, Jegen M, Micallef A (2020) Multi-layered high permeability conduits connecting onshore and offshore coastal aquifers. Front Mar Sci 7:531293
- Zhang S, Hu X, Han Z, Li J, Garzanti E (2018) Climatic and tectonic controls on Cretaceous-Palaeogene sea-level changes recorded in the Tarim epicontinental sea. Palaeogeogr Palaeoclimatol Palaeoecol 501:92–110

Publisher's Note Springer Nature remains neutral with regard to jurisdictional claims in published maps and institutional affiliations.

